Materials Science & Engineering R 135 (2019) 58–84

Contents lists available at ScienceDirect

Materials Science & Engineering R

journal homepage: www.elsevier.com/locate/mser

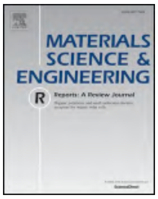

Zinc-ion batteries: Materials, mechanisms, and applications

Jun Ming[1], Jing Guo[1], Chuan Xia, Wenxi Wang, Husam N. Alshareef*

Materials Science and Engineering, Physical Science and Engineering Division, King Abdullah University of Science and Technology (KAUST), Thuwal, 23955-6900, Saudi Arabia

ARTICLE INFO

Keywords:
Zinc-ion batteries
Cathode
Electrolyte
Anode
Flexible batteries
Wearable devices

ABSTRACT

The increasing global demand for energy and the potential environmental impact of increased energy consumption require greener, safer, and more cost-efficient energy storage technologies. Lithium-ion batteries (LIBs) have been successful in meeting much of today's energy storage demand; however, lithium (Li) is a costly metal, is unevenly distributed around the world, and poses serious safety and environmental concerns. Alternate battery technologies should thus be developed. Zinc-ion batteries (ZIBs) have recently attracted attention due to their safety, environmental friendliness, and lower cost, compared to LIBs. They use aqueous electrolytes, which give them an advantage over multivalent ion batteries (e.g., Mg^{2+}, Ca^{2+}, Al^{3+}) that require more complex electrolytes. However, as with every new technology, many fundamental and practical challenges must be overcome for ZIBs to become commercial products. In this manuscript, we present a timely review and offer perspectives on recent developments and future directions in ZIBs research. The review is divided into five parts: (i) cathode material development, including an understanding of their reaction mechanism; (ii) electrolyte development and characterization; (iii) zinc anode, current collector, and separator design; (iv) applications; and (v) outlook and perspective.

1. Introduction

Most renewable energy sources, including solar, wind, tidal and geothermal, are intermittent by nature and thus require efficient energy storage systems to store the energy when renewable sources are not available [1–3]. Since the success of commercial LIBs by Sony Company in the 1990s, rechargeable lithium-ion batteries (LIBs) have dominated the energy market, ranging from handheld electronic devices and electric vehicles to intelligent grid storage [4–6]. However, the potential safety issues, high cost, and limited supplies of lithium (Li) still pose a significant challenge to the long-term viability of LIBs [7–9].

There has recently been a surge of interest in developing other kinds of mobile ion batteries, such as sodium- and potassium-ion batteries, due to the abundance of these elements and their low cost [10–12]. However, the high activity of Na and K still pose significant safety concerns, and their larger radii make it difficult to find appropriate cathode and anode materials that can reversibly accommodate these cations. Meanwhile, rechargeable, multivalent, metal-ion (Mg^{2+}, Ca^{2+}, Zn^{2+}, Al^{3+}) batteries have also attracted great attention, not only because they use earth-abundant polyvalent cations but also because of their improved safety and high volumetric energy density. However, the availability of compatible electrolytes for the reversible plating/stripping of Mg, Ca, or Al is still one of the main challenges facing such batteries, since current electrolytes cause the corrosion of metallic anode/current collectors and lead to the formation of inactive surface layers [13–16]. In addition, many of the proposed cathodes cannot easily accommodate the mobile cations because of a strong electrostatic interaction between multivalent metal ions and host cathodes.

In contrast, zinc-ion batteries (ZIBs), which consist of a zinc metal anode, a zinc-containing electrolyte, and a cathode for hosting Zn ions, are quickly gaining attention by many research groups. This is because of the following attractive features: (1) the diversity of potential electrolytes, including aqueous and non-aqueous electrolytes; (2) the higher redox potential of zinc (-0.763 V vs. a standard hydrogen electrode [SHE]), which can allows the battery to work in aqueous electrolytes [17], which is difficult to be realized for other mobile ion batteries; (3) the improved safety and reduced toxicity of ZIBs; and (4) the reversibility of Zn plating/stripping, where the near-neutral or slightly acidic electrolyte (e.g., pH = 3.6–6.0) can avoid the formation of zinc dendrites and ZnO byproducts, unlike the case of an alkaline Zn battery (e.g., $Zn + 4OH^- \leftrightarrow Zn(OH)_4^{2-} + 2e^- \leftrightarrow ZnO + 2OH^- + H_2O + 2e^-$) [18]. Therefore, a long cycle life can be achieved; (5) a higher volumetric energy density (i.e., 5855 mA h cm^{-3} compared to 2061 mA h cm^{-3} for LIBs) can be achieved due to the high density of Zn

---

* Corresponding author.
E-mail address: husam.alshareef@kaust.edu.sa (H.N. Alshareef).

[1] These authors contribute equally.

https://doi.org/10.1016/j.mser.2018.10.002
Received 16 September 2018; Received in revised form 6 October 2018; Accepted 23 October 2018

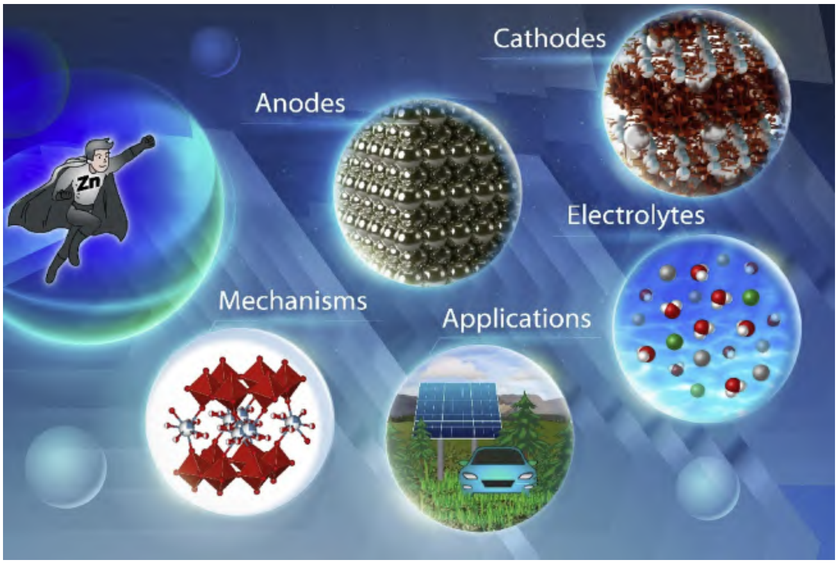

Fig. 1. Components and applications of zinc ion battery.

and the fact that two electrons are involved in the electrochemical reactions. Making ZIBs that are small in size is essential for deployment in miniaturized devices such as epidermal, implantable, and wearable sensors. All the above features mean that there is great potential for the commercialization of Zn-ion batteries.

However, fundamental knowledge in the cathode material intercalation of Zn, reaction mechanisms, and electrolyte performance as well as the details of the manufacturing process need to be better understood, scaled up, and made more reliable. In this article, we summarize the state of the art of Zn-ion batteries, and we provide a perspective about the important issues (Fig. 1) and future directions on which the community should focus to make the commercialization of ZIBs a reality. The review is divided into five parts: i) cathode material design, synthesis, and reaction mechanism; ii) electrolyte development and characterization; iii) zinc anode, current collector, and separator design; iv) ZIB applications in conventional and miniaturized applications; and v) prospects and perspectives.

2. Cathode materials and reaction mechanism

2.1. Manganese-based cathodes

To date, the most commonly studied cathode for ZIBs is manganese oxide (MnO_2), which exhibits a remarkable diversity of crystal structures and multivalent states of Mn. The performance and stability of a MnO_2 cathode for ZIBs has been found to strongly depend on its crystal structure. A summary of the comparative performance of the various crystalline structures of manganese oxide cathodes in ZIBs is presented in Fig. 2 [19–44]. It is interesting to see that the capacity of manganese oxide is quite different, even for compounds with the same chemical formula and crystal structure. The theoretical capacity of $Mn^{4+}O_2$ can be calculated as a starting point according to the step-wise reactions (i.e., $Mn^{4+}O_2 + Zn^{2+} + 2e^- \rightarrow ZnMn_2^{3+}O_4$, 308 mA h g^{-1}; $ZnMn_2^{3+}O_4 + Zn^{2+} + 2e^- \rightarrow 2ZnMn^{2+}O_2$, 308 mA h g^{-1}). These results demonstrate that MnO_2 can, in principle, deliver a capacity of 308 mA h g^{-1} and 616 mAh g^{-1} in the redox reaction Mn^{4+}/Mn^{3+} and Mn^{4+}/Mn^{2+}, respectively, (Fig. 2a), regardless of where the Zn^{2+} is finally located. Based on these two reactions and their corresponding capacities, we can understand the behavior of other MnO_2 cathodes with varying crystalline structures.

2.1.1. α-MnO_2 (2*2 tunnels)

Hollandite-type MnO_2 (α-MnO_2) is the most commonly studied manganese oxide (Fig. 3a), with a crystal structure that consists of MnO_6 octahedra connected by corner sharing in double chains. Although it has a symmetric tunnel structure of a [2 × 2] cross section, the reaction mechanism is still controversial. The Zn^{2+} (de-)intercalation mechanism within the partial crystalline α-MnO_2 ($\delta Zn^{2+} + 2\delta e^- + MnO_2 \leftrightarrow Zn_\delta Mn^{(4-2\delta)+}O_2$) was proposed for the first time in 2009 [19]. The ZIBs with the configuration of Zn/α-MnO_2 were introduced, and good (dis-)charge curves with a specific capacity of 210 mA h g^{-1} (i.e., $Zn_{0.68}Mn^{2.64+}O_2$) were demonstrated (Fig. 3a–c) [20]. Later, the formation of a new phase was confirmed by electrochemical impedance spectroscopy (EIS) [45], where a different intercalation process (i.e., $Zn^{2+} + 2e^- + 2Mn^{4+}O_2 \leftrightarrow ZnMn_2^{3+}O_4$) was proposed [21]. This speculation was proved by the reversible formation/disappearance of $ZnMn_2O_4$ during the (dis-)charge process, as observed by X-ray diffraction (XRD). In addition, the reversible variation of Mn^{4+}/Mn^{3+}, characterized by *ex-situ* synchrotron X-ray absorption spectroscopy (XAS), also supported this conclusion (Fig. 3d–e). All these results demonstrate reversible Zn^{2+} (de-)intercalation within α-MnO_2, with a capacity of approximately 200 mAh g^{-1}; however, the exact details of the intercalation process and discharge products are disputed.

For example, the presence of dissolved Mn^{2+} in electrolytes challenges the intercalation mechanism of ZIBs using α-MnO_2 cathodes. Oh *et al.* found that approximately one third of the total Mn in the cathode was dissolved in electrolytes [22]. A reversible phase transition between the tunneled α-MnO_2 and the layered Zn-birnessite ($Zn_\delta MnO_2$) was thus proposed (Fig. 4a). The formation of Zn-birnessite is a thermodynamically favorable process because the bridge-like double chains of $Mn^{3+}O_6$ units can be gradually destroyed as the dissolution of Mn^{2+} occurs (e.g., $MnO_2(s) + e^- \leftrightarrow Mn_2^{3+}O_3(s)$; $Mn_2^{3+}O_3(s) \leftrightarrow Mn^{4+}O_2(s) + Mn^{2+}(aq.)$) due to the Jahn-Teller effect. These results were confirmed by XRD and selected area electron diffraction (SAED) patterns (Fig. 4b–c) [22]. In addition, the discharged product was further confirmed by *in-situ* XRD [23], which revealed that the Zn-birnessite is formed by the loss of the intercalated Zn^{2+} and water molecules from the layers. However, we have to note that the theoretical capacity should be as high as 616 mAh g^{-1} due to the Mn^{4+}/Mn^{2+} redox reaction. Nevertheless, the measured capacity is only about 200 mAh g^{-1}, which means only 32.5% of α-MnO_2 has reacted.

In addition to the intercalation and phase transition mechanism, a precipitation process (i.e., $Zn^{2+} + SO_4{}^{2-} + 6OH\text{-} + 5H_2O \leftrightarrow Zn_4(OH)_6(SO_4){\cdot}5H_2O$ (s)) was also proposed, which leads to the confirmation of $Zn_4(OH)_6(SO_4){\cdot}5H_2O$ (ZHS) on the surface of α-MnO_2 [24] (Fig. 5). Moreover, there was no Zn^{2+} intercalation in α-MnO_2 because

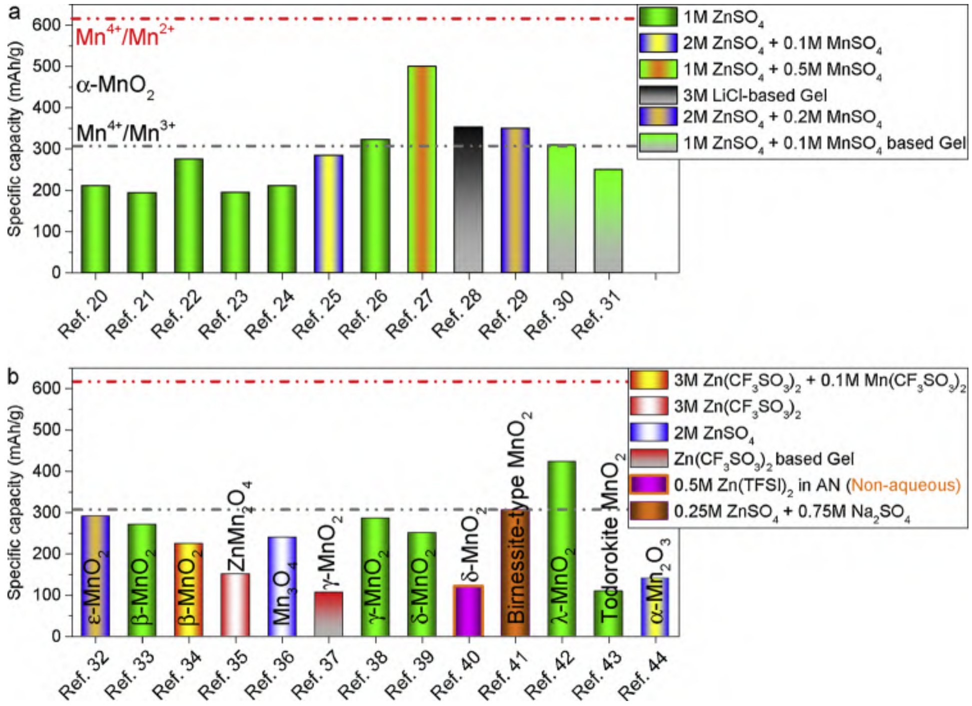

Fig. 2. Specific capacity of manganese oxide with different crystal structures and different electrolytes: (a) α-MnO_2, (b) other MnO_2 crystal structure.

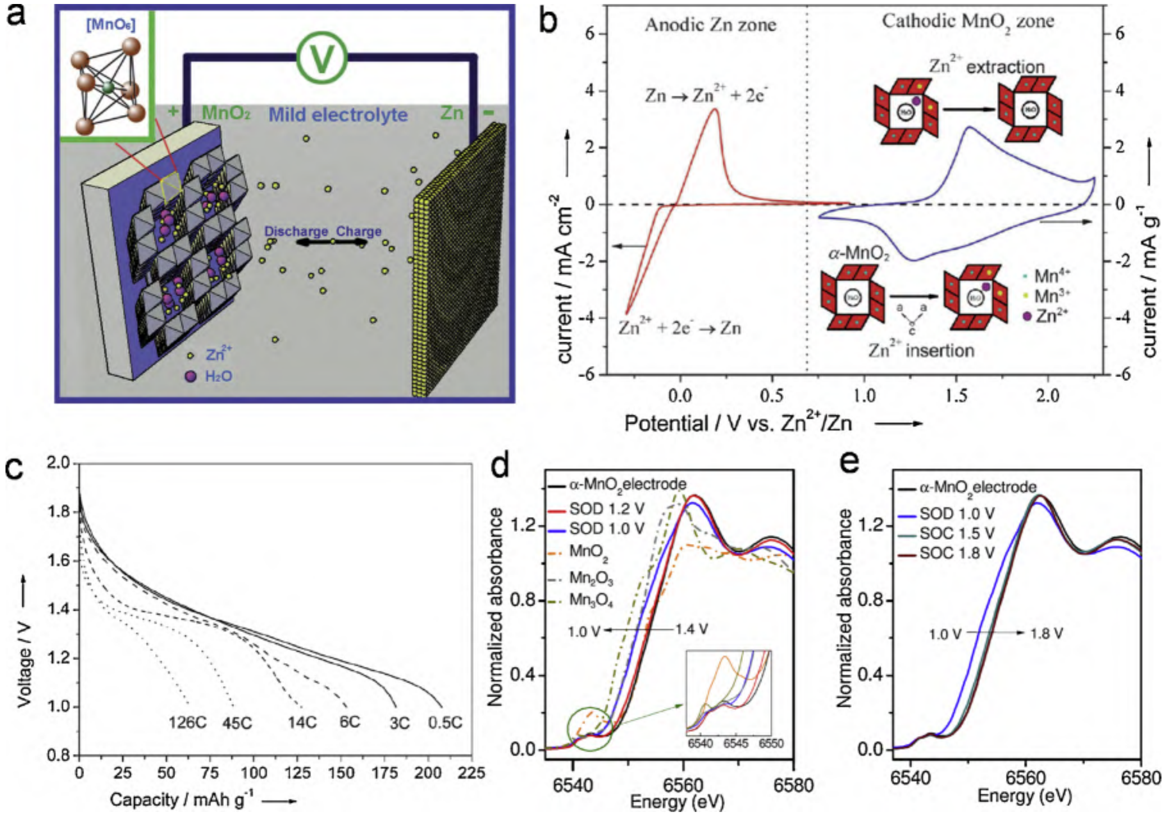

Fig. 3. Different Zn^{2+} (de)intercalation mechanisms in α-MnO_2. (a) Schematic chemistry of the ZIB. Zn^{2+} ions migrate between tunnels of an α-MnO_2 cathode and a Zn anode. The inset in the upper left corner depicts the basic structural unit of the MnO_6 octahedra of MnO_2. (b) Cyclic voltammogram of the zinc anode (red line) and the α-MnO_2 cathode (blue line). (c) Discharge curves of the ZIB measured at various rates. A rate of *n*C corresponds to a full discharge in 1/n h. (d, e) *Ex-situ* XANES and EXAFS spectra of an α-MnO_2 electrode recorded at various discharge/recharge states in zinc-ion cells. Reproduced with permission [20,21] (For interpretation of the references to colour in this figure legend, the reader is referred to the web version of this article).

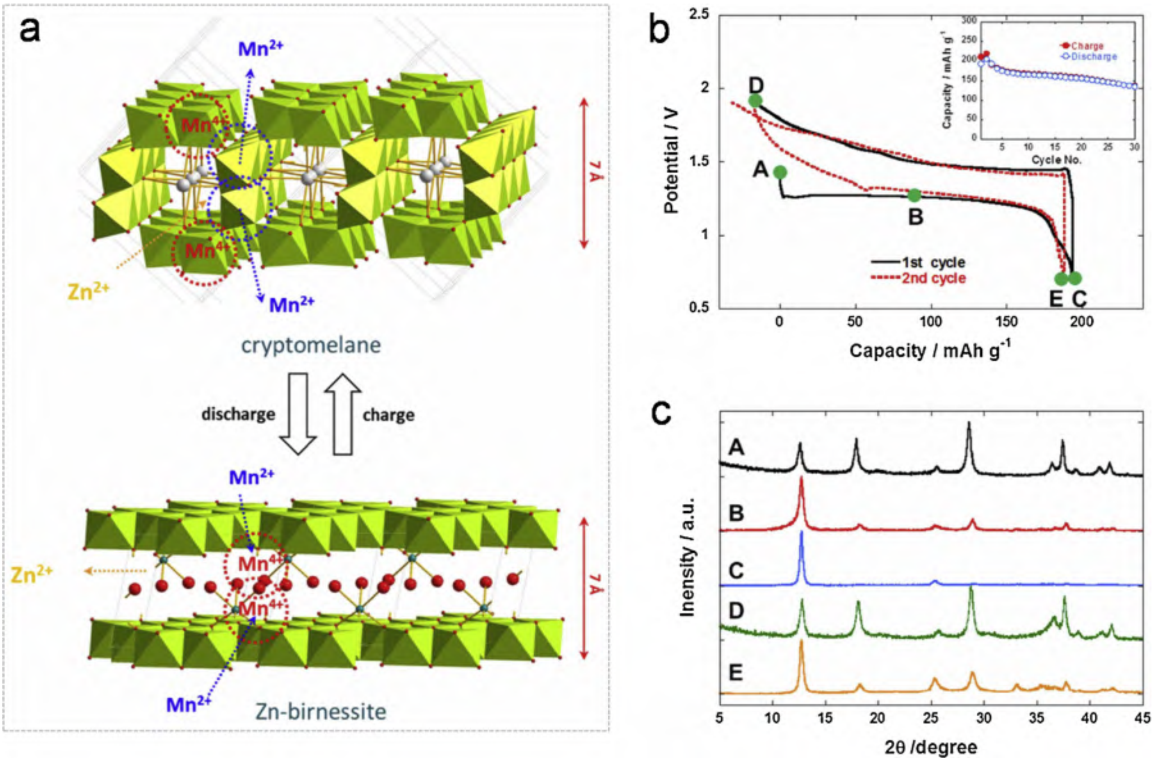

Fig. 4. Phase transition mechanism in α-MnO_2 during Zn^{2+} (de-)intercalation. (a) Schematic mechanism of zinc intercalation into α-MnO_2. (b) Potential profiles of the zinc/α-MnO_2 Zn-ion battery during the first (black line) and the second (red line) cycles, and their cycling performance up to 30 cycles (inset). (c) *Ex-situ* XRD patterns of the electrodes at various charge and discharge stages: original electrode (A), half-discharged electrode (B), fully discharged electrode (C), fully recharged electrode (D), and fully re-discharged electrode (E). Reproduced with permission [22] (For interpretation of the references to colour in this figure legend, the reader is referred to the web version of this article).

of the absence of Zn^{2+} within the α-MnO_2 cathode after washing off the ZHS layer. In this reaction, the hydroxide groups result from the pH variation with the dissolution of Mn^{2+} in electrolyte ($MnO_2(s) + 2H_2O \leftrightarrow Mn^{2+}(aq.) + 4OH$-), where the effect of pH variation on cations was *operando*-studied for the first time [24]. The mechanism of forming ZHS is supported by recent results, in which the ZHS was in fact used as a cathode directly [46]. Regardless of which mechanism takes place, it seems there is consensus that the capacity values are almost the same for α-MnO_2 (195–210 mA h g^{-1}).

Surprisingly, α-MnO_2 exhibited an exceptionally high rate capability, reaching as high as 126 C, as illustrated in Fig. 3c. The ZHS product can quickly form in solution; however, the conversion rate of α-$MnO_2(s)$ to $Mn^{2+}(aq.)$ cannot occur at such a rapid rate. Therefore, an H^+ intercalation mechanism within α-MnO_2 was proposed, in which

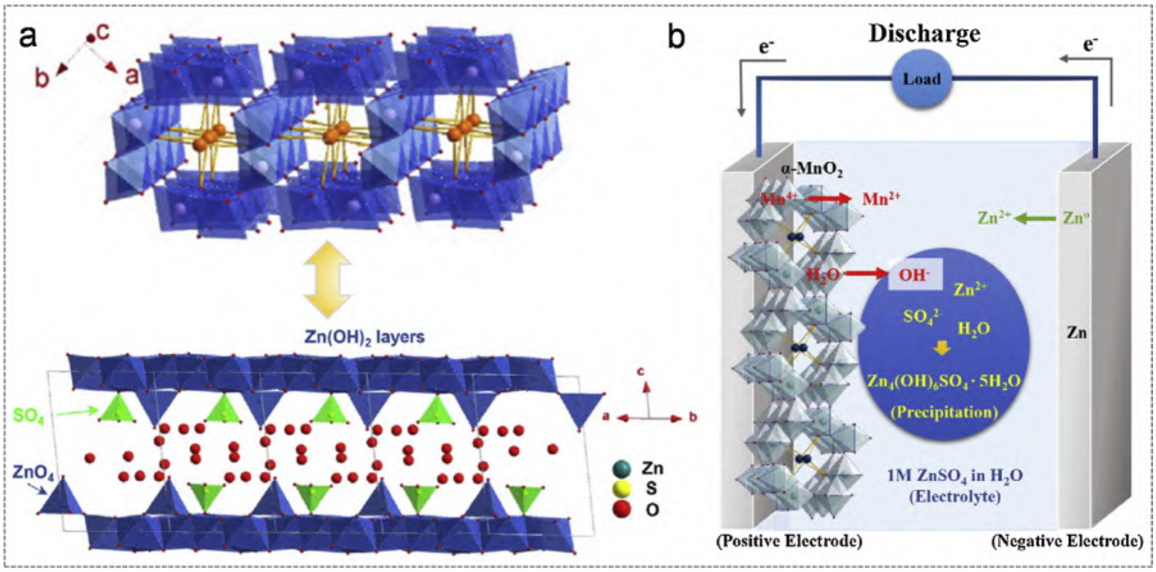

Fig. 5. Precipitation mechanism of α-MnO_2 during Mn^{2+} dissolution. (a) Schematic depiction of crystal structure conversion of α-MnO_2 and $Zn_4(OH)_6SO_4{\cdot}5H_2O$. (b) Schematic depiction of reactions that take place during the discharge process for an α-MnO_2/Zn cell employing an aqueous $ZnSO_4$ electrolyte. Zinc hydroxide sulfate precipitates as a result of a pH increase caused by Mn dissolution from the cathode. Reproduced with permission [24].

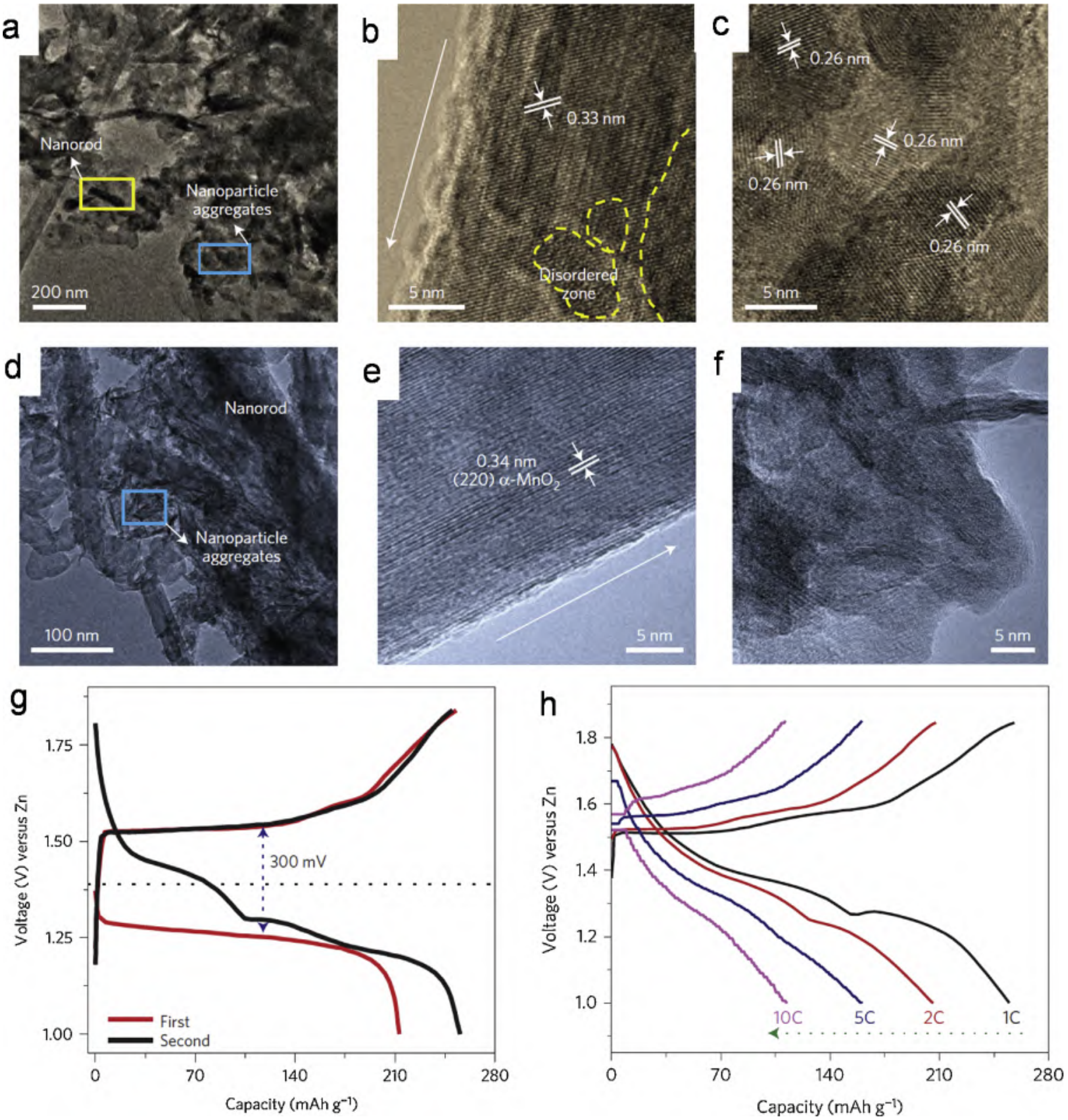

Fig. 6. H^+ (de-)intercalation mechanism within α-MnO_2. TEM/HRTEM images of MnO_2 electrodes discharged to (a–c) 1 V and then charged back to (d–f) 1.8 V in the first cycle. (g) Charge/discharge curves of a Zn/MnO_2 battery in the initial two cycles. (h) Rate performance. Electrolyte is a 2 M $ZnSO_4$ aqueous electrolyte with a 0.1 M $MnSO_4$ additive. Reproduced with permission [25].

MnOOH forms (i.e., $H_2O \leftrightarrow H^+ + OH^-$; $Mn^{4+}O_2 + H^+ + e^- \leftrightarrow Mn^{3+}OOH$), where the Zn^{2+} can react with hydroxide groups (OH^-) to form HZS (i.e., $1/2Zn^{2+} + OH^- + 1/6ZnSO_4 + 6/xH_2O \leftrightarrow 1/6ZnSO_4[Zn(OH)_3]{\cdot}xH_2O$) [25]. As a result, H^+ intercalation seems to be a reasonable way in which to interpret the fast reaction rates observed in α-MnO_2. The reversible conversion of α-MnO_2/MnOOH was confirmed by high resolution transmission electron microscopy (HR-TEM) according to the lattice spacing (Fig. 6a–f), and the presence of ZHS was confirmed by nuclear magnetic resonance (NMR) and XRD. In that study, a high capacity of 285 mA h g^{-1} was obtained (Fig. 6g–h), which is higher than previously reported capacities of around 200 mAh g^{-1}. This higher capacity could be due to the additives in the 0.1 M $MnSO_4$ electrolyte, as will be discussed in the electrolyte part. Note that high capacities of over 300 mA h g^{-1} were demonstrated for ZIBs using an α-MnO_2-based cathode with specific nanostructures, compositions, or battery configurations, such as nanostructured α-MnO_2 [26], α-MnO_2/CNTs [27], α-MnO_2/3D N−C [28], α-MnO_2/Graphene [29], and α-MnO_2/CNTs [30,31] in flexible batteries. Herein, we speculate that the dominant redox couple is Mn^{4+}/Mn^{2+}, otherwise the capacity could not reach over 308 mA h g^{-1}. It is clear that more work needs to be carried out to understand the reaction mechanism in α-MnO_2.

2.1.2. *ε-MnO_2*

The H^+ intercalation was also observed in akhtenskite-structure MnO_2 (ε-MnO_2) [32]. A successive H^+ and Zn^{2+} intercalation was verified by the galvanostatic intermittent titration technique (GITT) (Fig. 7a). Furthermore, the intercalation of H^+ and Zn^{2+} was proved using different electrolytes with and without H^+ and Zn^{2+} (Fig. 7b). Meanwhile, the presence of discharged products of $Mn^{3+}OOH$ and $ZnMn_2^{3+}O_4$ also support this conclusion (Fig. 7c). Benefiting from *the uniqueness of the structure and morphology* of ε-MnO_2, a high capacity of 300 mA h g^{-1}, close to the theoretical capacity of 308 mA h g^{-1}, was obtained through the Mn^{4+}/Mn^{3+} redox reaction. This type of electrodeposited ε-MnO_2 on carbon fiber paper (ε-MnO_2/CFP) displays an

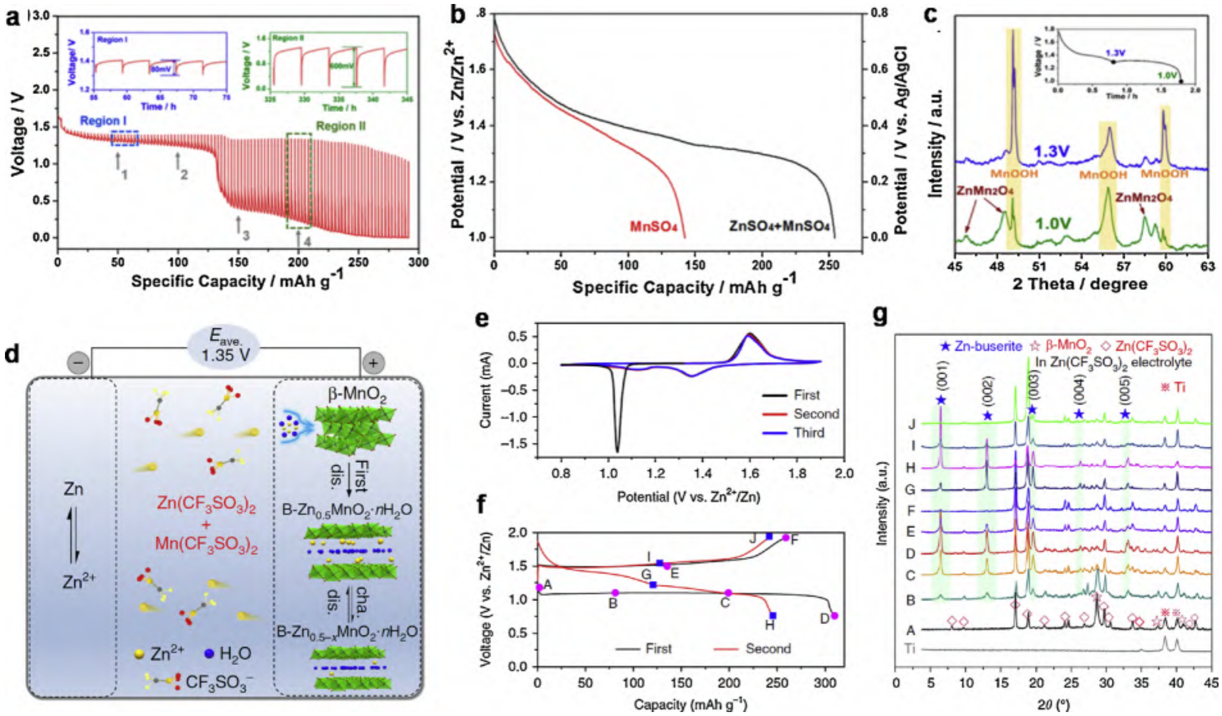

Fig. 7. H^+/Zn^{2+} co-intercalation within ε-MnO_2 and phase transition of β-MnO_2 during Zn^{2+} intercalation. (a) GITT profiles of MnO_2@CFP cathode, (b) discharge curves in 0.2 M $MnSO_4$ solution with or without $ZnSO_4$ as electrolytes, and (c) *ex-situ* XRD patterns at depths of discharge at 1.3 V and 1.0 V, respectively. Reproduced with permission. [32] Copyright 2016, American Chemical Society. (d) Rechargeable Zn/β-MnO_2 cell, (e) cyclic voltammograms, and (f) typical charge/discharge curves for the initial two cycles. The points A–J marked the states where data were collected for XRD analysis. (g) XRD patterns of a β-MnO_2 electrode at selected states during the first and second cycles. Reproduced with permission [34].

extremely long cycle life, with a 99.3% capacity retention after more than 10,000 cycles. Although the possibility of H^+/Zn^{2+} intercalation was confirmed, the reaction kinetics of H^+ and Zn^{2+} intercalation need to be further explored because of the different structure of ε-$Mn^{4+}O_2$ from the tunnel-type α-MnO_2.

*2.1.3. β-MnO_2 (1*1 tunnel)*

H^+ intercalation was reported in α-MnO_2 and ε-MnO_2; however, this phenomenon does not appear to occur in pyrolusite-type MnO_2 (β-MnO_2) due to the absence of MnOOH formation. Kim *et al.* demonstrated that Zn^{2+} can be intercalated into the β-MnO_2 framework even with the limited space of [1 × 1] tunnels, followed by the formation of Zn-inserted phases (e.g., $ZnMn_2O_4$, Zn-buserite, or Zn-birnessite) along with the precipitation of HZS on the electrode surface [33]. Chen *et al.* also confirmed the phase conversion of tunneled β-MnO_2 to layered Zn-buserite (B-$Zn_{0.5}Mn^{3+}O_2{\cdot}5H_2O$) during the first discharge, and then a reversible Zn^{2+} (de)intercalation occurred between B-$Zn_{0.5}Mn^{3+}O_2{\cdot}5H_2O$ and B-$Zn_{0.5\text{-}x}Mn^{(3-x)+}O_2{\cdot}5H_2O$ (Fig. 7d) [34]. The structural variation can be observed from the difference in CV characteristics and discharge-charge curves in the initial cycles (Fig. 7e–f). The results were also confirmed by XRD (Fig. 7g). The reaction mechanism of β-MnO_2 thus appears to involve a phase transition from a tunnel structure to layered Zn-buserite, with an initial capacity of around 250–270 mA h g^{-1}.

2.1.4. Spinel MnO_2 (3D structure)

Zn^{2+} and/or H^+ intercalation has been confirmed within hausmannite-type MnO_2. Such MnO_2 has a spinel structure, with Mn^{2+} (or Zn^{2+}) located in the tetrahedral sites and Mn^{3+} in the octahedral sites (e.g., $ZnMn_2^{3+}O_4$, $MnMn_2^{3+}O_4$) (Fig. 8a–d). Therefore, a charge process is a prerequisite because there is no space to accommodate the intercalated Zn^{2+} within the 3D structure with the reduction of Mn^{3+} to Mn^{2+}. The reaction mechanism of $ZnMn_{1.86}Y_{0.14}O_4 \leftrightarrow Zn_{1\text{-}x}Mn_{1.86}Y_{0.14}O_4 + 2xe + xZn^{2+}$ was recently confirmed in cation-deficient spinel $ZnMn_{1.86}Y_{0.14}O_4$ (ZMO, Y denotes vacancy) [35]. The results indicate that the Mn vacancies or deficiencies not only facilitate Zn^{2+} transport owing to the low electrostatic barrier, but also mitigate the dissolution of Mn species because of the higher mean Mn valence (+3.22) [47]. A moderate capacity of 150 mAh g^{-1} was delivered, and no structural evolution was observed (Fig. 8a, c). In contrast, a structural change was found in Mn_3O_4 (i.e., $Mn^{2+}Mn_2^{3+}O_4$). The Mn^{2+} in the tetrahedral sites was removed to form Mn_5O_8 ($2Mn_3O_4 \rightarrow Mn_5O_8 + Mn^{2+} + 2e$-), which was then transformed to birnessite-type MnO_2, triggered by the Mn^{2+} dissolution and H_2O insertion ($Mn_5O_8 + H_2O \rightarrow 4\,Mn^{4+}O_2{\cdot}xH_2O + Mn^{2+} + 2e$-) (Fig. 8b) [36]. The Zn-birnessite was thus formed upon Zn^{2+} intercalation during the discharge process, accompanied by the reduction of Mn^{4+} to Mn^{3+}. However, the MnOOH and HZS phases were observed, demonstrating that H^+ intercalation takes place. Therefore, the phase transition of Mn_3O_4 ($Mn^{2+}Mn_2^{3+}O_4$) to the layered birnessite is similar to that of β-$Mn^{4+}O_2$ [34], leading to a higher capacity of 239 mA h g^{-1} (vs. 150 mAh g^{-1} of ZMO) (Fig. 8d).

*2.1.5. γ-MnO_2 (1*1 and 1*2 tunnel)*

Nsutite-type MnO_2 (γ-MnO_2) is the first example of manganese oxide to be used for ZIBs in 2003 [37]. A reversible (de-)intercalation of Zn^{2+} was first proposed when a gel polymer electrolyte (GPE) and Zn$(CF_3SO_3)_2$ salt were used; however, a different H^+ intercalation mechanism was presented later in an aqueous electrolyte of $ZnSO_4$ and Zn$(NO_3)_2$ [20]. In 2014, Kim *et al.* presented a detailed Zn^{2+} (de-)intercalation process, in which the intermediates of spinel $ZnMn_2^{3+}O_4$/γ-$Mn^{2+}O_2$, spinel $ZnMn_2^{3+}O_4$/tunnel-type γ-$Zn_xMn^{2+}O_4$, and the final products of spinel $ZnMn_2^{3+}O_4$/tunnel-type γ-$Zn_xMn^{2+}O_4$/layered-type γ-$Zn_yMn^{2+}O_4$ were demonstrated (Fig. 9) [38]. The structural variation is reversible, and a high capacity of 285 mA h g^{-1} can be achieved. However, the cycle performance was not so optimal. The controversial Zn^{2+} or H^+ intercalation may be dependent on the crystal structure, which is an intergrowth between β-$Mn^{4+}O_2$ and ramsdellite-type R-MnO_2 with the co-existence of [1 × 2] and [2 × 2] tunnel structures.

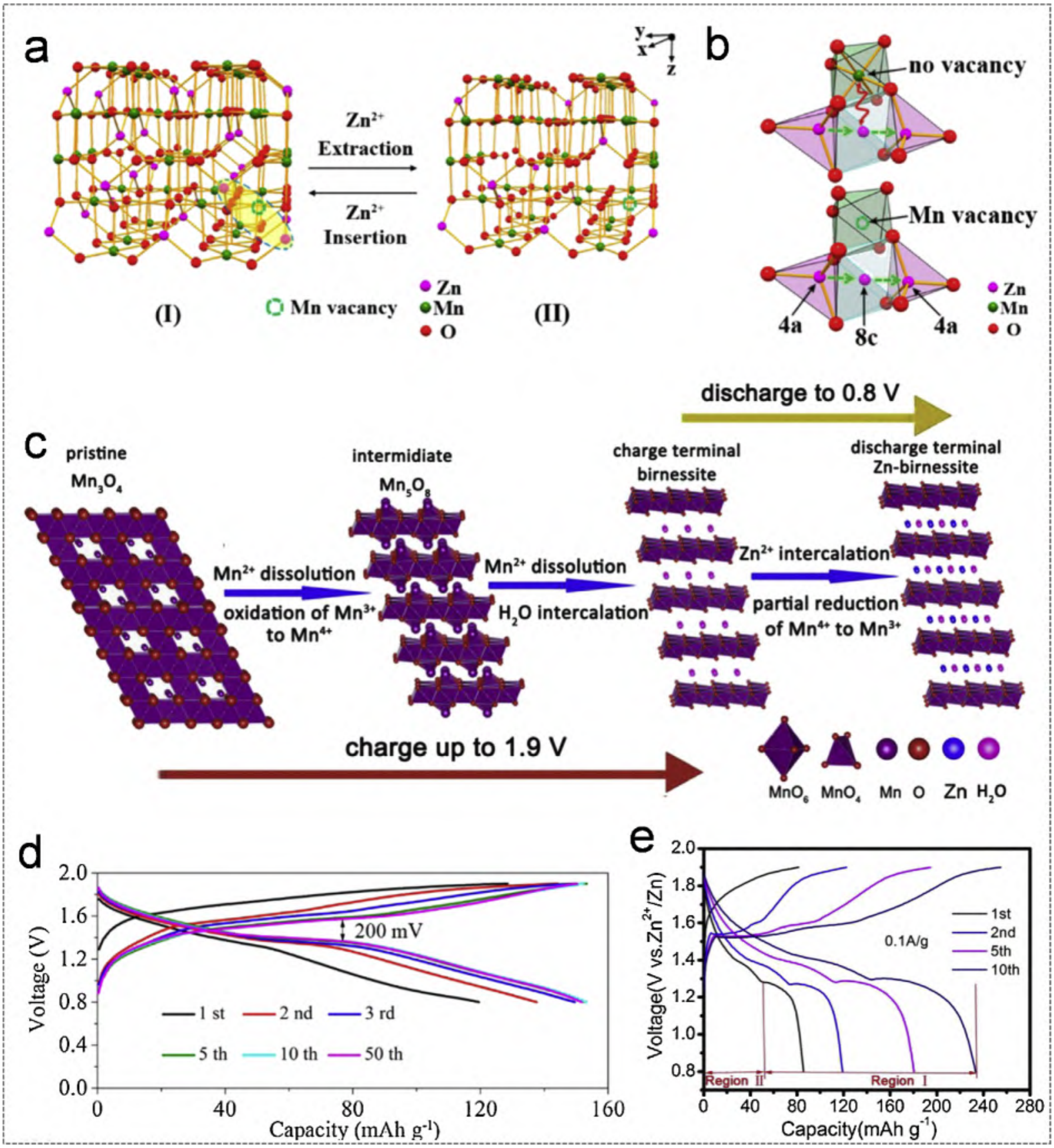

Fig. 8. Zn^{2+} and/or H^+ (de-)intercalation within spinel-structured MnO_2. (a) Schematic illustration of Zn^{2+} insertion/extraction in an extended three-dimensional ZMO spinel framework. (b) Proposed Zn^{2+} diffusion pathway in ZMO spinel without and with Mn vacancies. (c) Schematic reaction pathway of Mn_3O_4 within the first cycle. (d) Galvanostatic charge/discharge curves of ZMO/C at 50 mA g^{-1}. (e) Rate capability of Mn_3O_4. Reproduced with permission [35,36].

2.1.6. δ-MnO_2

In addition to β-MnO_2, layer-type MnO_2 (δ-MnO_2) is another case where H^+ intercalation is not observed. The Zn^{2+} can intercalate into the layered structure (which consists of sheets of MO_6 octahedra connected by edge sharing), similarly to Li^+ intercalation into Li-layered oxide cathodes (e.g., $LiCoO_2$) [48], However, a different structural evolution is observed as Zn^{2+} intercalation takes place because of the diversity of δ-MnO_2 phases (e.g., chalcophanite, birnessite, buserite, and vernadite), which leads to different cations and varying numbers of water molecules within the interlayer. For example, spinel-type $ZnMn_2^{3+}O_4$ (i.e., $2\delta\text{-}Mn^{4+}O_2 + Zn^{2+} + 2e^- \rightarrow ZnMn_2^{3+}O_4$) was found when nano-flake δ-MnO_2 was used in an aqueous electrolyte (Fig. 10a) [39], while a reversible variation of MnO_2/$ZnMnO_2$ was observed for hydrated δ-MnO_2 ($K_{0.11}Mn^{3.89+}O_2{\cdot}0.7H_2O$) in a non-aqueous electrolyte (Fig. 10b–c) [40]. The capacity of δ-MnO_2 in an aqueous electrolyte was found to be about 250 mAh g^{-1}, while that in a non-aqueous electrolyte is only about 120 mAh g^{-1} (Fig. 10a–c), confirming the considerable effect of a solvent in ZIBs. However, both capacities are lower than the theoretical value, demonstrating the limited utilization of MnO_2. A high capacity of 305 mA h g^{-1}, which is close to the theoretical value (308 mA h g^{-1}), was recently obtained; this is mainly due to the reversible Zn^{2+} (de-)intercalation within Zn-birnessite-type manganese oxide and the additional pseudocapacitive contribution of Na^+ [41].

2.1.7. Other Mn oxides

Although Zn^{2+} intercalation is speculated to be limited within λ-$Mn^{4+}O_2$ because of the limited 3D tunnels, a high capacity of

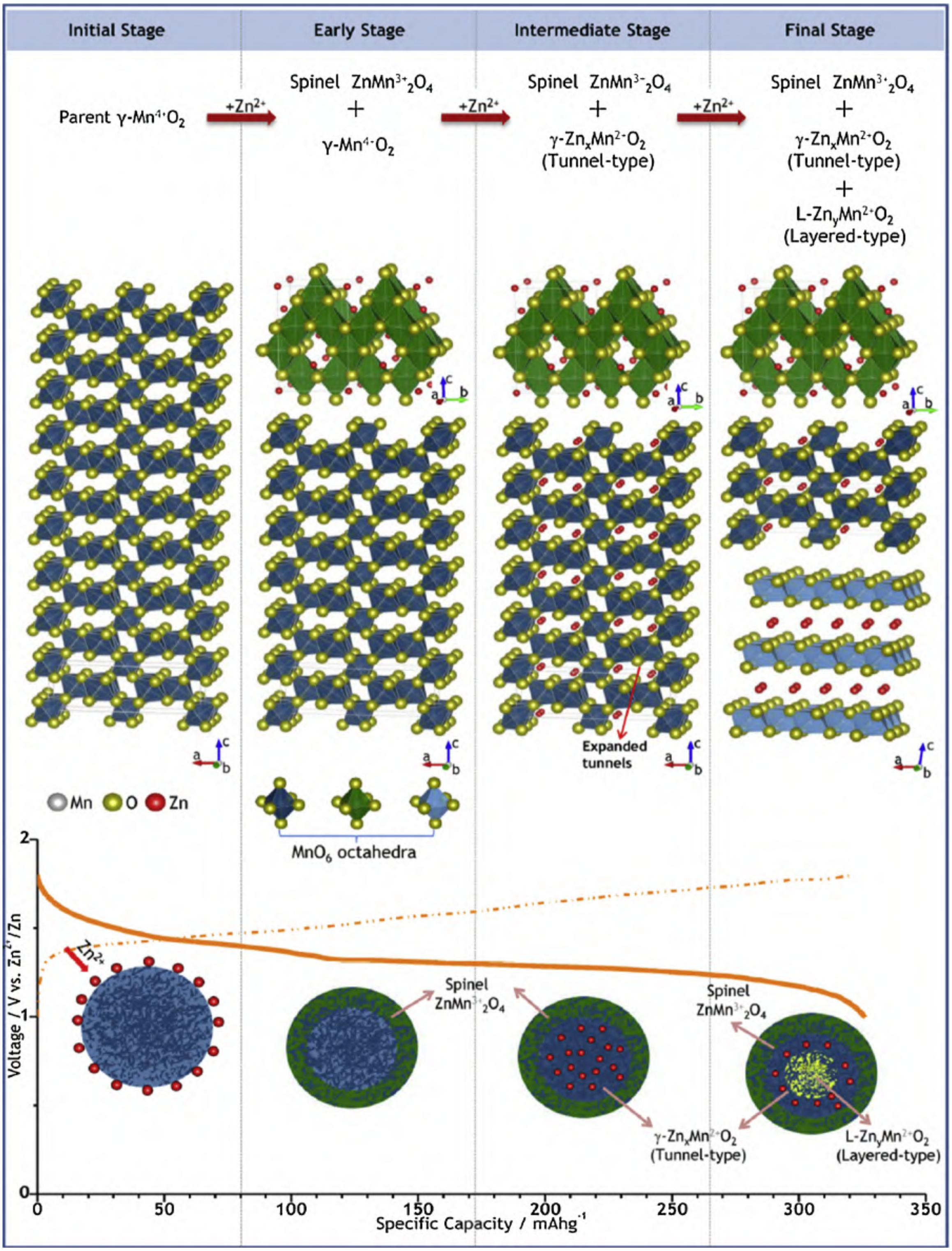

Fig. 9. Controversial Zn^{2+} or H^+ (de-)interaction mechanism within γ-MnO_2 and one typical phase transition. Schematic illustration of the reaction pathway of a Zn insertion in the prepared γ-MnO_2 cathode. Reproduced with permission [38].

442.6 mA h g^{-1} was reported for λ-$Mn^{4+}O_2$ prepared from the leaching of $LiMn_2O_4$ [42]. This means that the electrochemical performance is difficult to accurately predict based solely on the crystalline structure, since a phase transition may exist after the dissolution of Mn^{2+} during Zn^{2+} intercalation. This point is further confirmed in the case of todorokite-type MnO_2, which has a larger [3 × 3] tunnel and should in theory have a higher capacity to accommodate Zn^{2+}. However, only a low capacity of 108 mA h g^{-1} was obtained in the $Mg_{1.8}Mn_6O_{12}$·$4.8H_2O$ cathode [43]. The prevailing mechanism in this cathode is thus unclear at present; however, it is highly likely that only a small proportion of Mn^{4+} was reduced to Mn^{3+} or Mn^{2+}. In addition, the Zn^{2+} intercalation was confirmed within the $Mn^{3+}_2O_3$, where a transformation of bixbyite Mn_2O_3 to layered-type Zn-birnessite takes place upon the reduction of Mn^{3+} to Mn^{2+} (Fig. 10d) [44]. The measured capacity was about 140 mA h g^{-1} (Fig. 10e), demonstrating that less than half of the Mn^{3+} reacted during discharge. Finally, the phase transformations of

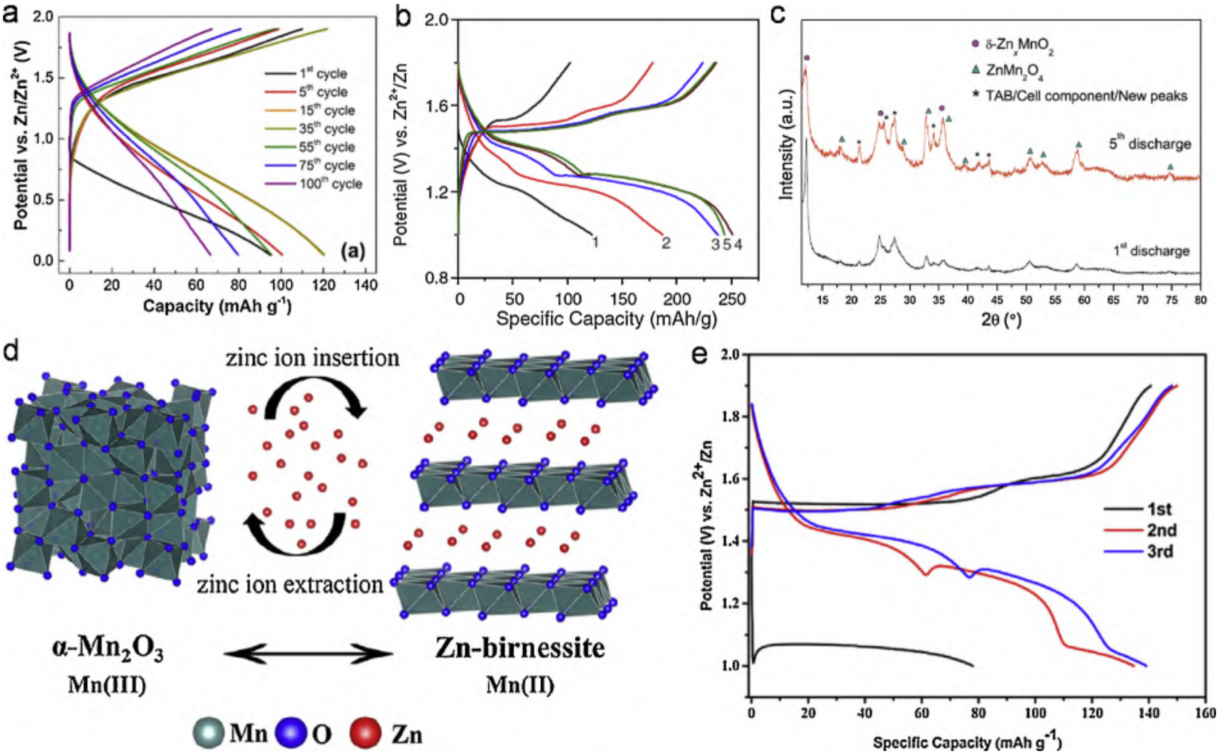

Fig. 10. Phase transition of δ-MnO_2 and other types of manganese oxide upon Zn^{2+} intercalation. (a) Potential vs capacity profiles of δ-MnO_2 using a non-aqueous AN-Zn$(TFSI)_2$ electrolyte. (b) Initial five voltage profiles of δ-MnO_2 using an aqueous electrolyte of 1 M $ZnSO_4$. (c) Ex-situ XRD patterns of the cathodes recovered from the Zn/δ-MnO_2 cells after the first and fifth discharge cycles. (d) Schematic Zn^{2+} (de-)intercalation within an α-Mn_2O_3 cathode and (e) a galvanostatic charge-discharge curve. Reproduced with permission [39,40,44].

most types of manganese oxide are summarized in Fig. 11. It can be seen that the reactions and conversion processes are complex, and more studies are needed to understand the intercalation processes in manganese oxides.

2.2. V-based cathodes

V-based cathodes for ZIBs offer two key advantages over Mn-based cathodes, including stability and diversity. Different from the typical MO_6 octahedral units occurring in MnO_2, V-O coordination polyhedra can adopt different units, including tetrahedron, trigonal bipyramid, square pyramid, distorted octahedron, and regular octahedron, which can change based on the V oxidation state [49,50]. As a result, a large family of vanadium oxides with different frameworks can be constructed by corner and/or edge sharing of these polyhedra, which allow for reversible Zn^{2+} (de-)intercalation. A summary of V-based cathodes used for ZIBs is compared in Fig. 12. The theoretical capacity of $V_2^{5+}O_5$ (i.e., $V_2^{5+}O_5 + Zn^{2+} + 2e^- \rightarrow ZnV_2^{4+}O_5$ is 147.4 mA h g^{-1}, and $V_2^{5+}O_5 + 2Zn^{2+} + 2e^- \rightarrow Zn_2V_2^{3+}O_5$ is 294.8 mA h g^{-1}) is calculated as a reference point to compare the measured electrochemical performance of various V-based cathodes. This is because V_2O_5 is the simplest and lowest molecular-weight V-based ZIB cathode.

2.2.1. Vanadium oxides

2.2.1.1. V_2O_5 and $M_xV_2O_5{\cdot}nH_2O$. The V_2O_5 and $M_xV_2O_5$ compounds (M = alkali, alkaline earth metals) generally consist of square pyramidal (VO_5) or octahedral (VO_6) units in which the V oxidation state can be varied from V^{5+} to V^{4+} or even to V^{3+} while maintaining the frameworks. The feasibility of Zn^{2+} intercalation into vanadium oxide can be judged from $Zn_xV_2O_5{\cdot}yH_2O$, which was prepared by the ionic exchange reaction between V_2O_5 and $ZnCl_2$ in an aqueous solution [51]. Later, the electrochemical intercalation of Zn^{2+}, comparable to that of Li^+ ions, was confirmed by cyclic voltammetric analysis [52]. While the fourfold coordination of Zn^{2+} with four apical oxygens in the V_2O_5 layer and the location of Zn^{2+} in quasi co-planar positions were confirmed by X-ray absorption spectroscopy (XAS) [53]. Several studies recently reported high performance V_2O_5 as a cathode for ZIBs [54–58]. Johnson *et al.* reported a high-power, rechargeable, non-aqueous, multivalent Zn/V_2O_5 battery with a reversible capacity of 170 mA h g^{-1} and a voltage at 0.85 V (Fig. 13a-b) [55]. Then, a hybrid ZIB of Zn/V_2O_5 using the concentrated Li/zinc salt electrolyte was introduced, giving rise to an increased capacity of 239 mA h g^{-1} [56]. This was the first time a hybrid-ion battery using concentrated electrolytes in ZIBs was introduced (Fig. 13c–d), and it triggered numerous follow-up studies [15,59,60]. However, the details of Li^+ and/or Zn^{2+} intercalation within V_2O_5 during the (dis-)charge process still need to be explored further. As the development of cathode material synthesis and electrolyte design improved, higher capacities of 372 mA h g^{-1} and 470 mA h g^{-1} were obtained for the $V_2O_5{\cdot}nH_2O$/Graphene [57] and $V_2O_5{\cdot}nH_2O$ [58], respectively, where the battery could cycle more than a few thousand cycles. Although high capacities were obtained, we should keep in mind that the capacity is much higher than the theoretical 294.8 mA h g^{-1} calculated based on the V^{5+}/V^{3+} variation of the V oxidation state.

The framework stability of V_2O_5-based compounds can be further improved by introducing cations and water molecules within the layer of V_2O_5 (e.g., $Zn_{0.25}V_2O_5{\cdot}nH_2O$). As illustrated in Fig. 14, Nazar *et al.* reported that the interlayer of $Zn_{0.25}V_2O_5{\cdot}nH_2O$ (10.8 Å) could increase to 12.9 Å after being immersed in an electrolyte and then reduced to 11 Å during discharge [61]. This occurred because the water molecules were inserted into the cathode and expanded its layer spacing before the discharge, but were removed upon Zn^{2+} intercalation during discharge, thereby reducing the interlayer spacing of the cathode. Reversibly, the de-intercalation of Zn^{2+} and the insertion of water molecules can be observed in the following charge process (Fig. 14a-b). In this study, a high capacity of 300 mA h g^{-1} was obtained with a voltage

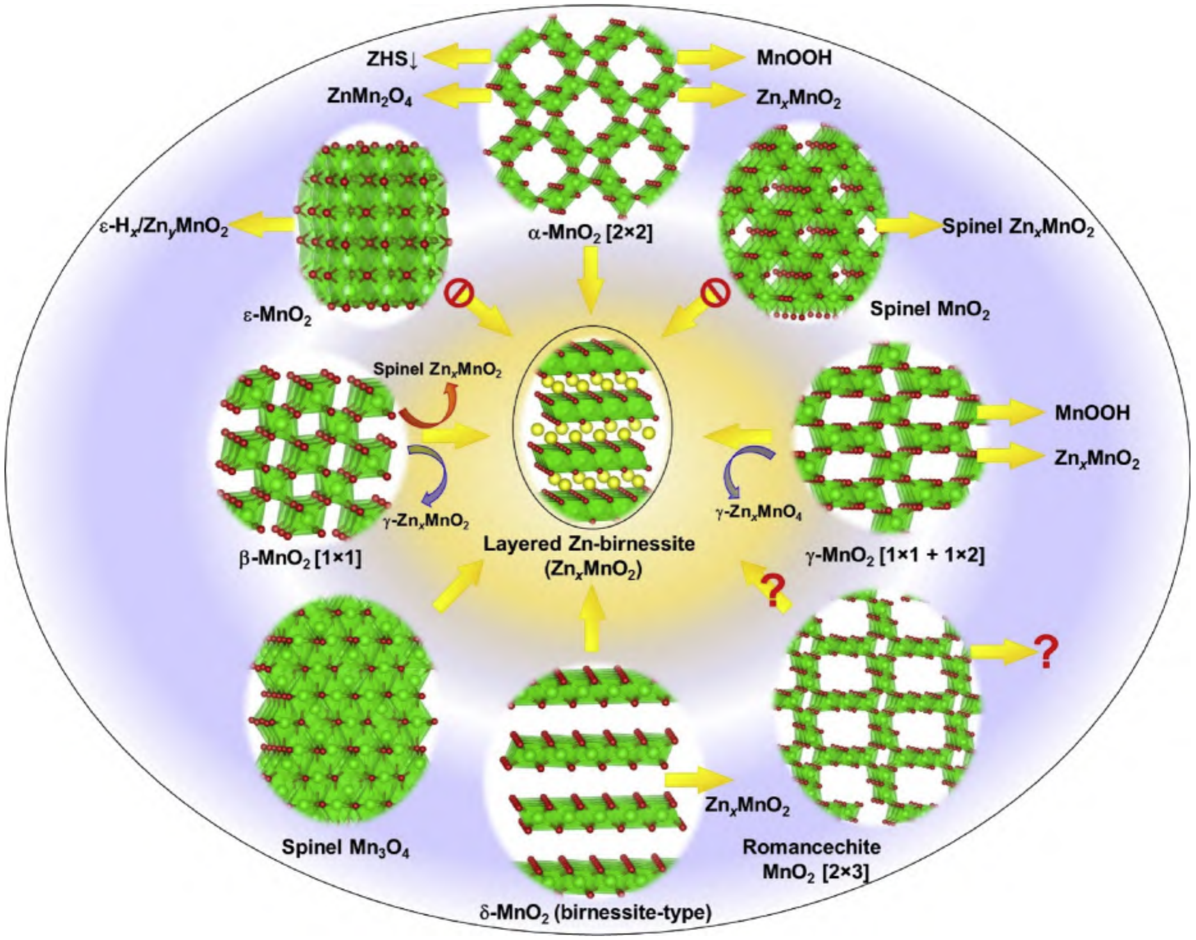

Fig. 11. A summary of phase transition and conversion of most manganese oxides. The green octahedral is MnO_6, in which the red and yellow dots represent oxygen and zinc atoms, respectively. The arrows pointing to the center means that there is a phase transition to layered Zn-birnessite. (For interpretation of the references to colour in this figure legend, the reader is referred to the web version of this article).

of 0.85 V (Fig. 14c), where more than one Zn^{2+} per formula unit can be involved in the reaction even at an extremely high rate.

It is speculated that the interlayer spacing can be further enlarged if other types of cations with larger radii were located within the cathode interlayers. $Ca_{0.24}V_2O_5{\cdot}0.83H_2O$ represents a prime example that has been recently used as a cathode in ZIBs [62]. In this compound, one Ca atom coordinates with four coplanar oxygen atoms from the water and three apical oxygens from the V_2O_5 layers to form CaO_7 polyhedra (Fig. 15a) [63]. A larger interlayer spacing was therefore obtained with hydrated water, as demonstrated by XRD and TGA analysis (Fig. 15b-d). Benefiting from the unique morphology of $Ca_{0.24}V_2O_5{\cdot}0.83H_2O$ nanobelts and fourfold higher electrical conductivity than $Zn_{0.25}V_2O_5{\cdot}nH_2O$, a high capacity of 340 mA h g^{-1} at 0.2 C and 155 mA h g^{-1} at 30 C was achieved (Fig. 15e-h). Furthermore, 76% of the capacity of this cathode material was demonstrated to be capacitive in nature (Fig. 15i), thereby explaining the reason for a higher capacity than the theoretical value. Another useful feature of $Ca_{0.24}V_2O_5{\cdot}0.83H_2O$ is its extremely long cycle life, where over 8000 cycles were shown. The stability of $M_xV_2O_5{\cdot}nH_2O$ is further confirmed in the case of $Na_{0.33}V_2O_5$, in which the quadruple octahedral chains are linked by double chains of square pyramids through sharing their corners [64]. Although a new phase of $Zn_xNa_{0.33}V_2O_7$ appeared and a large capacity decay existed in the initial two cycles due to the crystal distortion and presence of Zn^{2+} in "dead sites," a reversible high capacity of 270 mA h g^{-1} at ~0.70 V could be maintained over 1000 cycles. In addition to the Zn^{2+}-, Ca^{2+}-, and Na^{+}-doped V_2O_5-based compounds, two other derivate compounds, namely $K_2V_8O_{21}$ and $Ag_{0.4}V_2O_5$, displayed capacities of around 247 mA h g^{-1} [65,66].

2.2.1.2. $M_xV_3O_8$. The $M_xV_3O_8$ (M = alkali ion or H) compounds are composed of VO_6 octahedra and VO_5 square pyramids, where the difference in crystalline structure depends on which corner these two kinds of polyhedra share. Herein, we classify two types of structures according to their connectivity: **(1)** edge-sharing octahedral (VO_6) and square pyramidal (VO_5) chains constructing the V_3O_8 layers along the z axis by sharing their corners, with the alkali ions (e.g., Li^{+}, Na^{+}) located in the interstitial sites linking the V_3O_8 layers together, thereby giving rise to $LiV_3^{5+}O_8$ or $NaV_3^{5+}O_8$ [67]; **(2)** VO_6 and VO_5 connected to each other by different ways to form V_3O_8 layers, where an H atom is bonded to the oxygen of VO_6 octahedra [68]. Therefore, $H_2V_3O_8$ (i.e., $V_3O_7{\cdot}H_2O$) consists of V^{5+} and V^{4+} in a ratio of 2:1. As a result, the average voltage plateau of LiV_3O_8 and NaV_3O_8 (i.e., 0.75 V, V^{5+}/V^{3+}) is higher than ~0.60 V of $H_2V_3O_8$ (i.e., $V^{(14/3)+}/V^{3+}$) as Zn^{2+} (de-)intercalation occurs due to the difference of V oxidation state.

The layered-type LiV_3O_8 (LVO) is confirmed to experience a solid-solution behavior where Zn^{2+} intercalation changes the cathode to $ZnLiV_3O_8$, $ZnLiV_3O_8$-$Zn_yLiV_3O_8$ to the final $Zn_yLiV_3O_8$ ($y \geq 1$) during discharge (Fig. 16a) [69]. The Zn^{2+} (de-)intercalation is reversible, and a specific capacity of 172 mA h g^{-1} could be achieved (Fig. 16c). However, the cycling performance of this type of V_2O_5-based compound displayed only 75% capacity retention in the initial 65 cycles. For the $Na_xV_3O_8{\cdot}yH_2O$ cathode, superior capacities of 352 mA h g^{-1} and 361 mA h g^{-1} were obtained for the cathodes $NaV_3O_8{\cdot}1.63H_2O$ [70] and $Na_2V_6O_{16}{\cdot}3H_2O$ [71], respectively. The Zn^{2+} (de-)intercalation is reversible, and a high rate capacity of up to 2000 mA g^{-1} was observed (Fig. 16b, d). Note that the cycle performance of

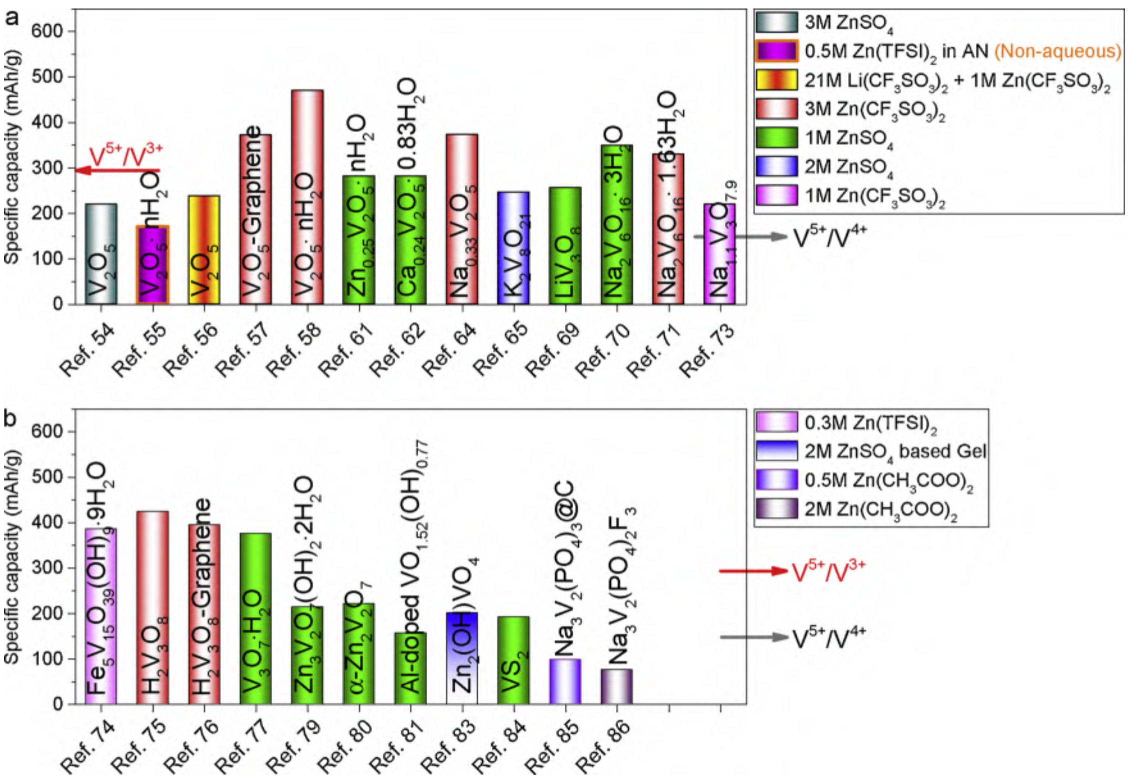

Fig. 12. Specific capacities of ZIBs using V-based cathode materials with different crystal structures and electrolytes.

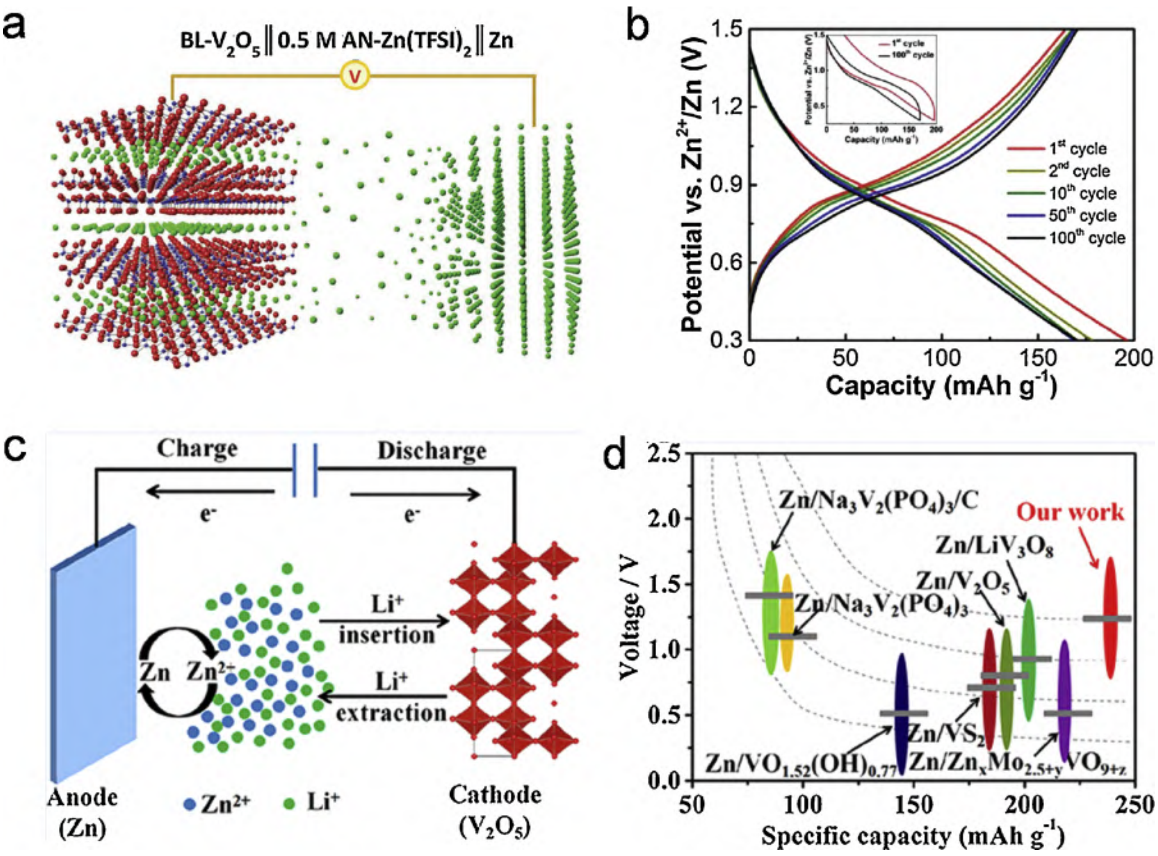

Fig. 13. Electrochemical performance of V_2O_5-based cathode. (a) Schematic depiction of a Zn/BL-V_2O_5 cell (red: oxygen, green: zinc, blue: vanadium). (b) Potential versus capacity profiles. (c) Schematic illustration of a Zn/V_2O_5 aqueous hybrid-ion battery. (d) Comparison of porous V_2O_5 with a recently reported vanadium-based cathode for ZIBs in terms of specific capacity and voltage platform. Reproduced with permission [55,56] (For interpretation of the references to colour in this figure legend, the reader is referred to the web version of this article).

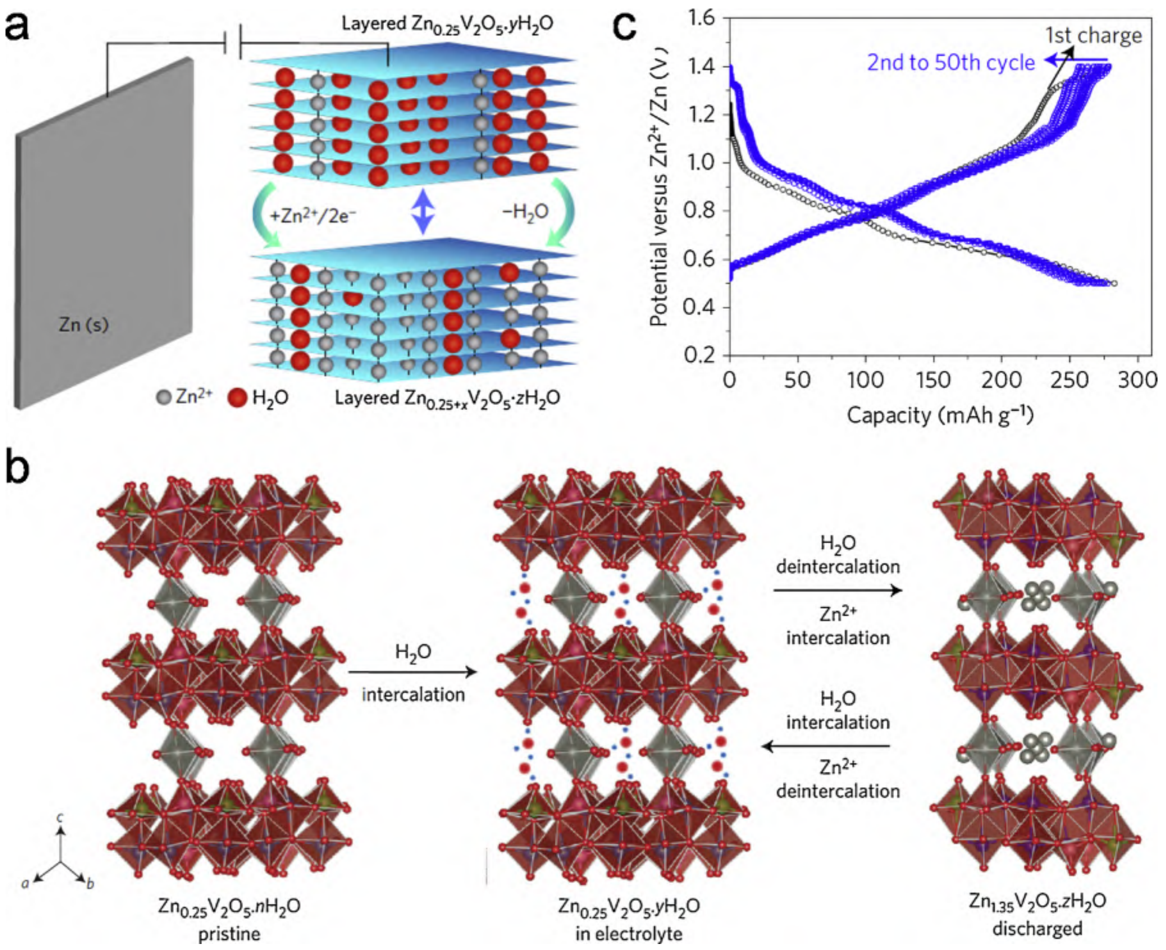

Fig. 14. Electrochemical performances of $Zn_{0.25}V_2O_5\cdot nH_2O$ and structural variation during Zn^{2+} intercalation. (a) Schematic depiction of the Zn metal/$Zn_{0.25}V_2O_5$ cell in discharged state in aqueous 1 M $ZnSO_4$. (b) Galvanostatic discharge and charge profiles at a 1 C rate and (c) structural variation of $Zn_{0.25}V_2O_5\cdot nH_2O$ as Zn^{2+} (de-)intercalation. Reproduced with permission [61].

$NaxV_3O_8\cdot yH_2O$ is much better than LVO [72], and this may be ascribed to the existence of intercalated water molecules in the interlayers. The vital role of crystal water to improve stability is further confirmed by the compound $Na_{1.1}V_3O_{7.9}$/graphene [73] and the $Fe_5V_{15}O_{39}(OH)_9\cdot 9H_2O$ nanosheet [74], which display capacities of 225 mA h g^{-1} and 385 mA h g^{-1}, respectively. Benefiting from the crystal water, the $H_2V_3O_8$ could deliver a high capacity of around 375–400 mA h g^{-1} and exhibit an extremely high rate capability, even up to 20 C, with a capacity of 250 mAh g^{-1} (Fig. 17) [75–77]. A detailed characterization confirmed that Zn^{2+} (de-)intercalation is reversible and that a new phase of $Zn_2V_3O_7\cdot H_2O$ was formed during the discharge process [77].

2.2.1.3. $M_xV_2O_7$.

The crystalline structure of $M_xV_2O_7$ consists of connected $[V_2O_7]$ groups along the z-axis, in which five-coordinated $[ZnO_5]$ and water molecules within the layer can stabilize the frameworks [78]. Two kinds of chemical compounds, including $Zn_3V_2^{5+}O_7(OH)_2\cdot H_2O$ [79] and α-$Zn_2V_2^{5+}O_7$ [80] with nanowire morphology, have recently been studied in ZIBs. A high capacity of 213 mA h g^{-1} at 50 mA g^{-1}, a capacity retention of 68% at 200 mA g^{-1} over 300 cycles, and a robust rate capability even up to 3000 mA g^{-1} were demonstrated for $Zn_3V_2O_7(OH)_2\cdot H_2O$ (Fig. 18) [79], while for the α-$Zn_2V_2O_7$ [80], an average capacity of 220 mAh g^{-1} was delivered, where 81% capacity retention was maintained at 4000 mA g^{-1} over 1000 cycles. Furthermore, the voltage could be maintained as high as 0.75 V on the merit of the initial V^{5+} oxidation state. Note that HZS, which was always observed in the case of Mn-based cathodes, was found in the discharged products for the first time in these two cathodes. The formation of HZS can generally be triggered when H^+ intercalation exists during discharge. Therefore, more studies are needed to confirm whether H^+ or Zn^{2+} intercalation is preferred.

2.2.1.4. M_xVO_2 and M_xVO_4.

Hollandite-type $V_{1-x}Al_xO_{1.52}(OH)_{0.77}$, derived from the chemical compound of $M^{z+}{}_xV^{(4-x\times z)+}O_2$ with a [2 × 2] tunnel structure composed of a square pyramid, was also applied as a cathode in ZIBs [81]. An improved capacity of 156 mA h g^{-1} and cycle performance were confirmed in Al-doped $V_{1-x}Al_xO_{1.52}(OH)_{0.77}$ due to the stabilization effect of stronger Al-O bonds in the crystal structure. However, the work voltage around at ~0.6 V (i.e., V^{4+}/V^{3+} redox reaction) is still low even after Al doping. A higher voltage of 0.75-0.8 V with a capacity of 205 mA h g^{-1} was obtained recently in the compound of $M_x^{z+}V^{(8-x\times z)+}O_4$ such as $Zn_2(OH)V^{5+}O_4$ [82,83].

2.2.2. Other V-based materials

Other V-based cathodes such as vanadium sulfide (e.g., VS_2) [84] and vanadium phosphate (e.g., $Na_3V_2(PO_4)_3$ [85], $Na_3V_2(PO_4)_3F_3$ [86]) have recently been applied in ZIBs. The $V^{4+}S_2$ is a typical layered transition-metal di-chalcogenide (TMD) with an interlayer spacing of 5.76 Å, in which the Zn^{2+} can be intercalated to form $Zn_{0.09}VS_2$ and then $Zn_{0.23}VS_2$ in discharge. A high capacity of 190.3 mA h g^{-1} and a robust rate capability were demonstrated (Fig. 19a-b), while the voltage around 0.6 V (i.e., V^{4+}/V^{3+} redox reaction) is somewhat low compared to that of V_2O_5-based compounds [84]. Benefiting from the stable

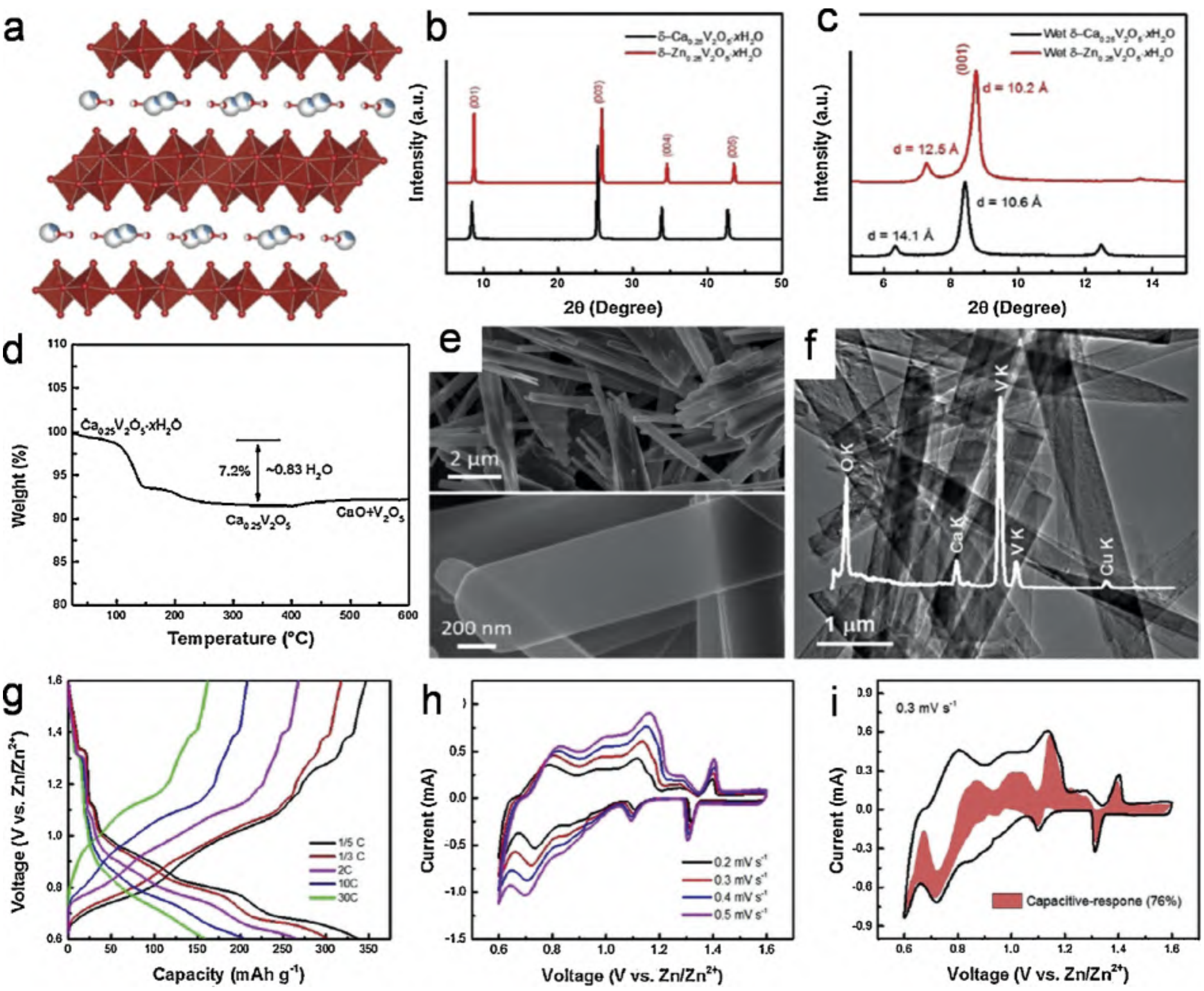

Fig. 15. Electrochemical performance of $Ca_{0.24}V_2O_5{\cdot}0.83H_2O$ (CVO). (a) Crystal structure viewed along the b-axis of CVO. (b, c) XRD pattern and (d) TGA results of as-synthesized CVO. (e–f) SEM and TEM images of CVO nanobelts. Inset in (f) is the EDS spectrum CVO. (g) Galvanostatic charge-discharge profiles at different current densities. (h) Cyclic voltammetry curves recorded at various scan rates. (i) Capacity separation analysis at 0.3 mV s^{-1}. The red-shaded data show the contribution to capacitive charge storage as a function of potential. Reproduced with permission [62] (For interpretation of the references to colour in this figure legend, the reader is referred to the web version of this article).

NASICON structure, the Na^+ in the $Na_3V_2(PO_4)_3$ can be extracted, and the framework of $NaV_2(PO_4)_3$ can accommodate Zn^{2+} ions reversibly with V^{4+}/V^{3+} redox reactions [85]. This cathode exhibits a specific capacity of 97 mA h g^{-1} with a high voltage of 1.0 V (Fig. 19c-d) [85]. The higher voltage (vs. 0.6 V of VS_2) is ascribed to the larger electronegativity difference of V-O than that of V-S in the V^{4+}/V^{3+} redox reaction. To seek a higher voltage, the NASICON $Na_3V_2(PO_4)_3F_3$ is an ideal candidate because of the higher oxidation state of $V^{4.5+}$ and larger electronegativity resulting from the fluoride ion [87]. As a result, an impressive voltage of 1.65 V with a capacity of 61 mA h g^{-1} was demonstrated (Fig. 19e).

In summary, the capacity and stability of most V-based cathodes are higher than those of Mn-based cathodes because the capacitive contribution to overall capacity is larger, and the structures are inherently more stable. However, the voltage of the V-based compound is approximately 0.75 V, which is lower than ~1.3 V often obtained for Mn-based cathodes. Therefore, there is still room for improvement of the V-based cathodes for ZIBs.

2.3. Prussian blue analog-based cathode

A high voltage can be achieved in ZIBs in which Prussian blue analogs (PBAs)—$MFe(CN)_6$ (M = Fe, Co, Ni, Cu, Mn)—are used, where $F(III)C_6$ and MN_6 octahedra are linked by $C{\equiv}N$ bridges to form an open 3D framework [88]. The PBAs refer to the transition-metal hexa-cyanoferrates (MHCFs), and different types of PBAs can be prepared by varying the metal (M). Up to now, NiHCF, CuHCF, and FeCHF with the typical cubic structure and ZnHCF with a rhombohedral framework have been studied as cathodes for ZIBs. The relative performance of PB compared with other ZIB cathodes is summarized in Fig. 20.

The exploration of $Zn_3[Fe(CN)_6]_2$ (i.e., ZnHCF) as a cathode in ZIBs was proposed in 2015 [89]. A high operation voltage of 1.7 V with a capacity of 65.4 mA h g^{-1} was achieved (Fig. 21a-b). The results reveal that 0.85 mol Zn^{2+} can intercalate into ZnHCF and that the performance can be further improved through controlling the morphologies and exposed facets [90]. Furthermore, a higher voltage of 1.73 V was demonstrated in the CuHCF nanoparticles (Fig. 21c-d) [91], but with a low capacity of 56 mA h g^{-1} and a cycle life around 100 cycles [92]. The capacity decay was initially ascribed to the materials dissolution, affected by the electrolyte and current density [93]. Later, a phase transition and nucleation within CuHCF was confirmed to be the root cause [94]; however, more details about the phase transformation should be investigated. For example, the structural changes associated with the possibility of Zn^{2+} swapping positions between the tunnels and the vacant $Fe(CN)_6$ sites in the CuHCF has recently been confirmed by operando synchrotron XRD [94], whereas for the FeHCF, an impressive capacity of 120 mAh g^{-1} was achieved through the Fe^{3+}/Fe^{2+} redox reaction (Fig. 21e) [95,96]. However, the voltage of FeHCF is

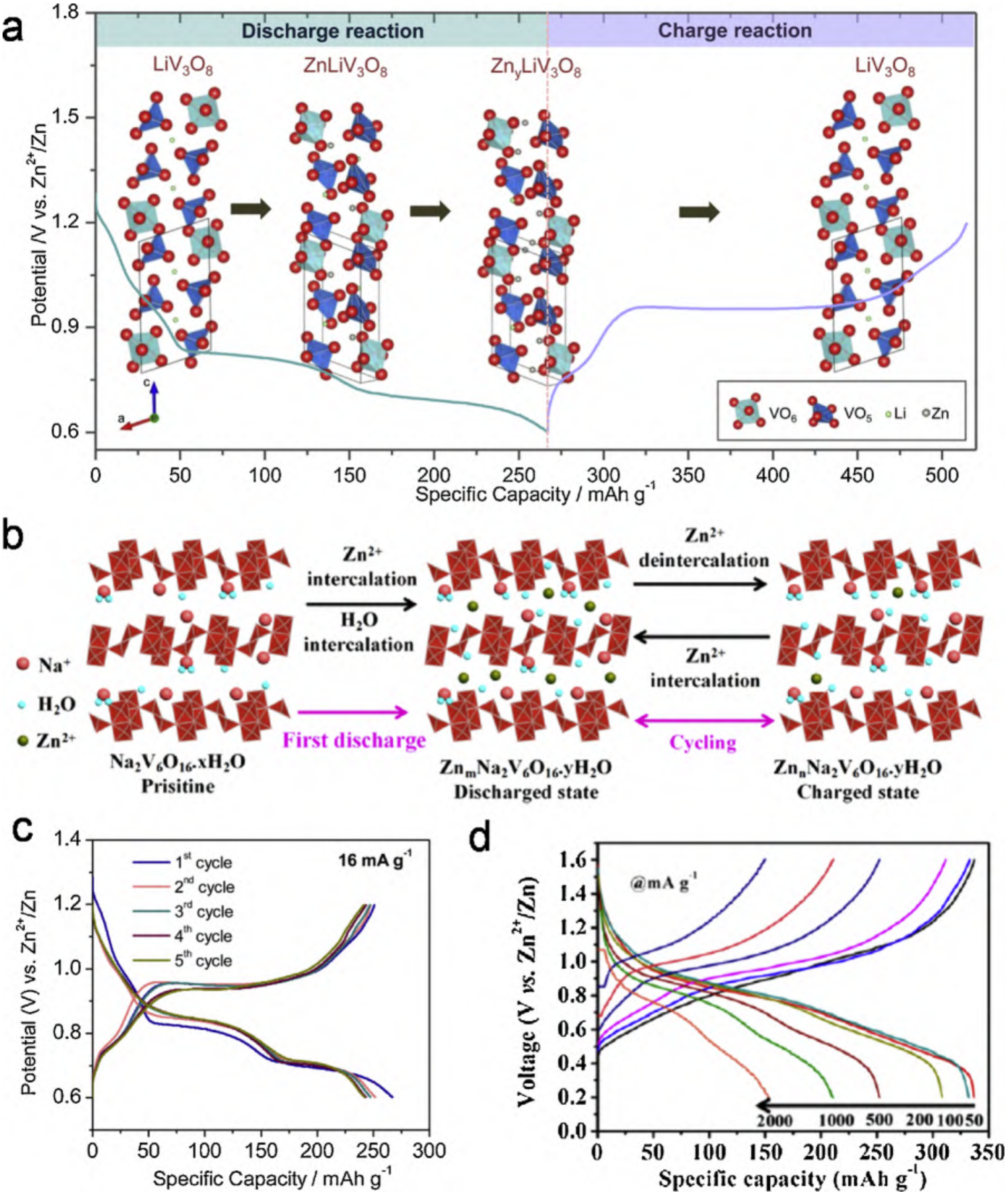

Fig. 16. Zn^{2+} (de-)intercalation mechanism within $M_xV_3O_8$ (M = Li^+, Na^+). Schematic depiction of the Zn^{2+} (de-)intercalation mechanism in (a) the LiV_3O_8 and $NaV_3O_8 \cdot 1.63H_2O$ cathode. (b) Initial five voltage profiles of the LVO electrode at a current density of 16 mA g^{-1}. (c) Charge-discharge curves of the $NaV_3O_8 \cdot 1.63H_2O$ at various current densities, ranging from 50 to 2000 mA g^{-1}. Reproduced with permission [69,70].

~1.1 V, which is lower than ~1.7 V obtained for ZnHCF and CuHCF. In addition, the potassium nickel hexacyanoferrate $K_{0.86}Ni[Fe(CN)_6]_{0.954}(H_2O)_{0.766}$ (KNF-086) [97] demonstrates a limited voltage plateau around 1.2 V and a low capacity of ~56 mA h g^{-1} even though the Zn^{2+} (de-)intercalation is reversible.

To improve the performance of PBA cathodes in ZIBs, a new rechargeable Na-Zn hybrid aqueous battery has been introduced. In this design, Na^+ rather than Zn^{2+} (de-)intercalation occurs within the NiHCF cathode, and a Zn/Zn^{2+} redox reaction occurs at the zinc anode in the (dis-)charge process. Benefiting from this hybrid concept [98], the battery can cycle more than 1000 cycles with a higher capacity of 76.2 mA h g^{-1} and an operational voltage close to 1.5 V (Fig. 22a-b) [99]. Alternatively, the composite of ZnHCF@MnO_2 with a wrapped structure has also been introduced (Fig. 22c), in which the unique structure can modulate the Zn^{2+} storage because of the incorporation of the capacitive and intercalative properties of both components together with the redox reactions [100]. A high capacity of 118 mA h g^{-1} and a voltage of 1.7 V were thus achieved on the merits of these synergistic effects (Fig. 22d). These two strategies can be widely extended to seek more reliable battery configurations and performances.

2.4. Spinel-structured oxide

Operational voltage is critical to pursue a high energy density in

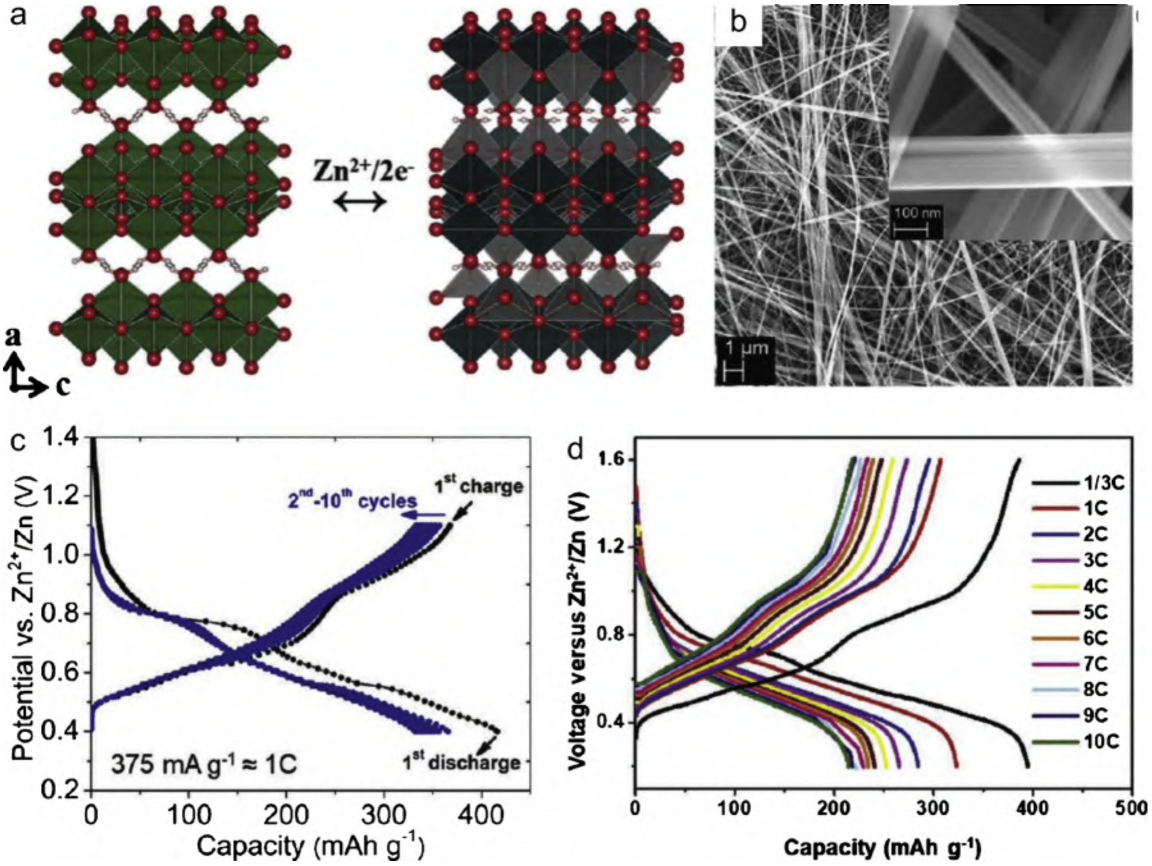

Fig. 17. Zn^{2+} (de-)intercalation behavior within $H_2V_3O_8$. (b) Crystal structure viewed along the [010] direction, showing the large interlayer gallery between V_3O_7 sheets perpendicular to the [100] direction for Zn^{2+} intercalation. VO_x polyhedra are depicted in green and blue for the pristine and the Zn^{2+} intercalated materials, respectively. ZnO_x polyhedra, gray; O, red spheres. (b) SEM image of the $H_2V_3O_8$ nanofibers. (c) Galvanostatic discharge and charge profiles of the $V_3O_7{\cdot}H_2O$ freestanding cathode at 1 C. (d) Galvanostatic charge-discharge profiles of $H_2V_3O_8$/graphene at different C rates. Reproduced with permission [76,77] (For interpretation of the references to colour in this figure legend, the reader is referred to the web version of this article).

rechargeable batteries, while the average voltage in ZIBs is limited. Although PBA-based cathodes display a voltage as high as 1.7 V, they still suffer from poor cycling performance and structural stability. A new series of spinels, $ZnAl_xCo_{2-x}O_4$ (Fig. 23a) [101], were recently reported as cathodes for ZIBs. This new spinel compound demonstrates a high voltage of 1.7 V, and it can cycle more than 100 cycles with a capacity of 114 mA h g^{-1}, in which the Zn^{2+} can intercalate into the spinel structure reversibly, accompanied by the reversible Co^{4+}/Co^{3+} conversion within the lattice (Fig. 23b). In addition, Al^{3+} doping can stabilize the spinel structure due to the stronger Al-O bonds—an effect that was also observed in the compound $V_{1-x}Al_xO_{1.52}(OH)_{0.77}$ [81]. Analogous to $LiNi_{0.8}Co_{0.15}Al_{0.05}O_2$ (NCA) in LIBs [102], the compound $ZnNi_xMn_xCo_{2-2x}O_4$ may be another compound that is suitable as a cathode for ZIBs [103]. As a result, the new spinels of $ZnNi_xMn_xCo_{2-2x}O_4$ (x = 1/2) were prepared and cycled over 200 cycles as cathodes in ZIBs (Fig. 23c–e) [104]. The obtained capacity was about 174 mA h g^{-1}, and the voltage was as high as 1.8 V. Multiple reversible conversion reactions involving Co^{4+}/Co^{3+}, $Ni^{4+}/Ni^{3+}/Ni^{2+}$, and Mn^{4+}/Mn^{3+} oxidation states were observed in the Zn^{2+} (de-)intercalation, and a superior rate capability was demonstrated. The ZIBs using such spinel compounds and zinc anodes are promising not only thanks to improved safety over Li, but also thanks to a high energy density of ~305 Wh kg^{-1} (vs. cathode), which is the highest energy density yet reported for a Zn-intercalated cathode. However, the performances of these new spinels were not studied in an aqueous electrolyte.

2.5. Organic and other cathode materials

Organic electrodes have recently attracted great attention in rechargeable batteries because the organic network can readily buffer the structural variation and give rise to a long cycle life (Fig. 20). The 9, 10-di(1,3-dithiol-2-ylidene)-910-dihydroanthracene (exTTF) was the first organic electrode used as a cathode in ZIBs [105]. A high capacity of 130 mA h g^{-1} with a voltage of 1.05 V was demonstrated, and a long lifespan over 10,000 cycles was achieved (Fig. 24a). Furthermore, a quinone electrode was recently introduced, in which the Zn^{2+} can be stored in quinone compounds through coordination with the negatively charged oxygen atoms in the electrochemically reduced carbonyl groups. The process is named an "ion-coordination" mechanism, where the calix [4]quinone (C4Q) delivers a high capacity of 335 mA h g^{-1}, a relatively high voltage of 1.0 V, and a lone cycle life over 1000 cycles (Fig. 24b-c) [106]. Note that the polarization in (dis-)charge curves is as low as 0.07 V, where the flat voltage plateau is similar to that of lithium iron phosphate ($LiFePO_4$) [107]. However, the dissolution of discharged products and the poisoning of the zinc anode by quinone limit the cycle life. Moreover, poly(benzoquinonyl sulfide) (PBQS) was also used as a cathode in ZIBs, and the redox reactions of PBQS molecules can be regarded as the reversible bonding of Zn^{2+} ions with O atoms in PBQS (Fig. 24d) [108]. As a result, a high capacity of 203 mA h g^{-1} with an average voltage of 0.9 V was demonstrated. This concept of using polymer-based cathodes in ZIBs can be widely extended. In addition to the organic and aforementioned inorganic cathodes, another compound of Mo_6S_8 was also used as a cathode for Zn^{2+} (de-)intercalation. The process from Mo_6S_8 over $ZnMo_6S_8$ to $Zn_2Mo_6S_8$ in the

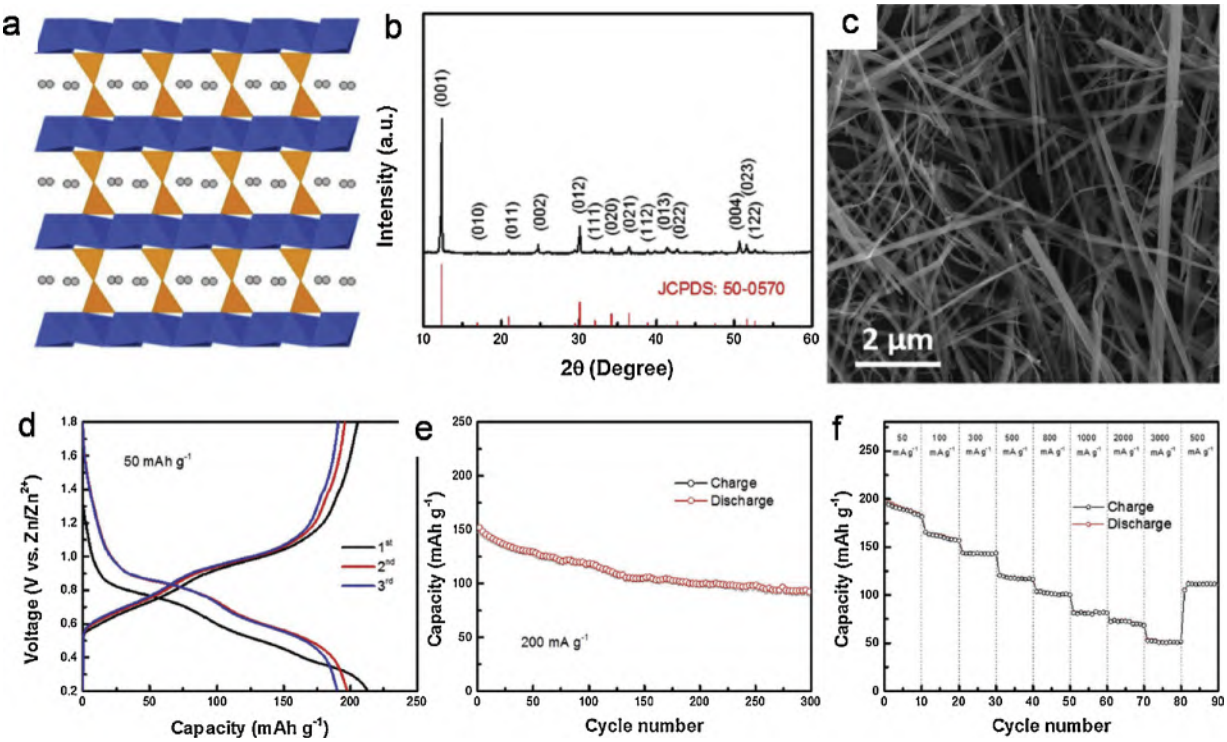

Fig. 18. Zn^{2+} (de-)intercalation behaviors within $M_xV_2O_7$ (e.g., $Zn_3V_2O_7(OH)_2{\cdot}2H_2O$ ZVO). (a) Crystal structure of ZVO viewed along the *b*-axis of ZVO. The Zn atoms in ZnO_6 and the V atoms in V_2O_7 polyhedra are depicted in blue and yellow, respectively. The gray atoms in the crystal cavities represent the lattice water. (b) XRD pattern and (c) SEM images of ZVO nanowires. (d) Galvanostatic charge-discharge profiles for ZVO electrodes at a current density of 50 mA g^{-1}. B) Cycle performance at a current rate of 200 mA g^{-1}. C) Rate capability of the ZVO cathode. Reproduced with permission [79] (For interpretation of the references to colour in this figure legend, the reader is referred to the web version of this article).

discharge and charge is reversible; however, the voltage around 0.35 is somewhat low, even though a capacity of 90 mA h g^{-1} can be delivered [109]. The same low-voltage cathode was also found in the chemical compound of $Zn_xMo_{2.5+y}VO_{9+z}$ [110], which has a voltage of ~0.2 V with a capacity of 220 mAh g^{-1}. While these chemical compounds are not particularly attractive due to the low voltage, they may be

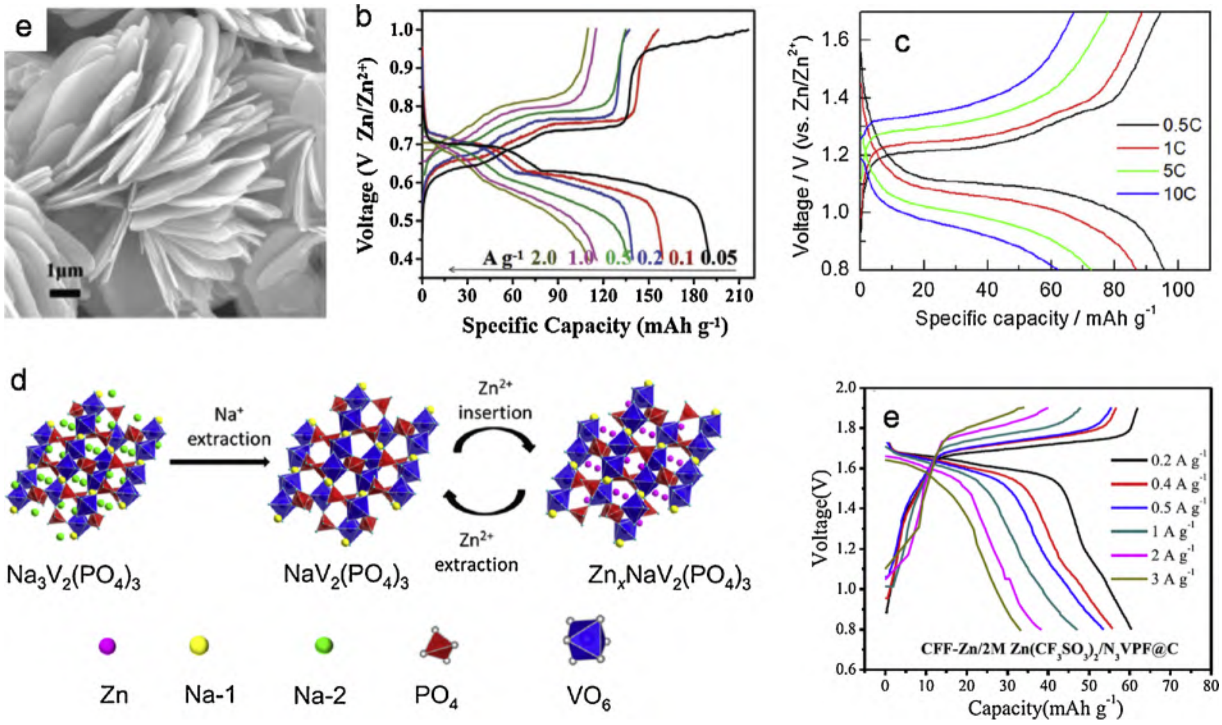

Fig. 19. Zn^{2+} (de-)intercalation behaviors in other V-based compounds. (a) SEM image and rate capability of VS_2. (b) Charge-discharge curves at different C rates and Zn^{2+} intercalation mechanism within NASICON $Na_3V_2(PO_4)_3$. (d) Rate capability of NASICON $Na_3V_2(PO_4)_2F_3$ battery. Reproduced with permission [84–86].

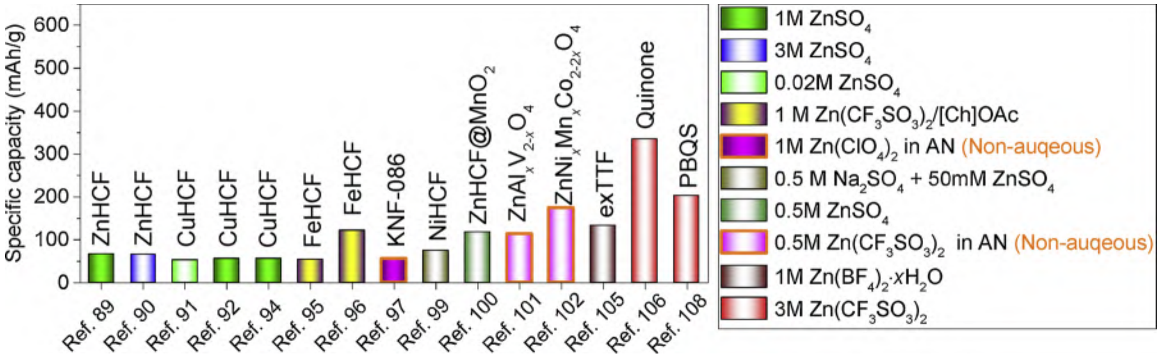

Fig. 20. A summary of the specific capacities of PBAs and other cathodes in different electrolytes.

candidates for storing Zn^{2+} as anodes.

Based on the above analysis, we can now compare the average capacity and voltage for the various reported ZIB cathodes: MnO_2 (240 mAh g^{-1}, ~1.3 V) > V-based cathode (245 mA h g^{-1}, ~0.75 V) > new spinel oxide (170 mA h g^{-1}, ~1.6 V) > organic cathode (335 mA h g^{-1}, ~1.0 V) > PBAs (~70 mA h g^{-1}, 1.7 V), in which the V-based compound demonstrates the best stability.

3. Electrolyte development and characterization

3.1. Electrolyte development

Aqueous electrolytes have dominated research on ZIBs because they are safer and cheaper, and they provide better stability for both anodes and cathodes. Furthermore, a neutral or mildly acidic aqueous electrolyte is preferred for ZIBs because zinc dendrite and ZnO can form more easily in alkaline aqueous electrolytes, while a strong acidic electrolyte can corrode the zinc anode and current collector. Up to now, different zinc salts, including $ZnSO_4$, $Zn(CF_3SO_3)_2$, $Zn(NO_3)_2$, $Zn(TFSI)_2$, $Zn(CH_3COO)_2$, $Zn(ClO_4)_2$, $Zn(BF_4)_2{\cdot}xH_2O$, ZnF_2, and $ZnCl_2$, have been widely investigated as ZIB electrolytes. These electrolytes are summarized in Fig. 2, Fig. 12, and Fig. 20. Among these, $ZnSO_4$ and $Zn(CF_3SO_3)_2$ are the most commonly used because of their stability and compatibility with the electrodes. However, $Zn(CF_3SO_3)_2$ is significantly more expensive than $ZnSO_4$, which may limit its commercial viability. $Zn(NO_3)_2$ was initially used with various ZIB cathodes, including MnO_2 [20,111,112], V_2O_5 [54], and PBAs [93]. However, its inferior performance [54] and its degradation of Zn anodes and CuHCF cathodes were observed due to the strong oxidant property of the nitrate ions [93]. The $Zn(CH_3COO)_2$ salt was investigated with various cathodes, including $Na_3V_2(PO_4)$ [85], $Na_3V_2(PO_4)_3F_3$ [86], FeHCF [95,96], and $Na_{0.95}MnO_2$ [113]. On the other hand, $Zn(TFSI)_2$ salt was tested with the cathodes δ-MnO_2 [40], $V_2O_5{\cdot}nH_2O$ [55], and $Fe_5V_{15}O_{39}(OH)_9{\cdot}9H_2O$ [15] [74]. Due to the inferior structural stability of MHCFs, the salt of $Zn(ClO_4)_2$ was further investigated for the cathodes of CuHCF [93] and NiHCF [97]; however, a large polarization was observed, which could be ascribed to the formation of a ZnO layer on the zinc anode surface. Although the salt $ZnCl_2$ was successfully used in a gel electrolyte for flexible batteries [114], the narrow anodic potential window limits its further applications [115]. Other salts, such as $Zn(BF_4)_2{\cdot}xH_2O$, were studied in the organic electrode exTTF [105], while the low solubility of ZnF_2 in water was limited [93]. Finally, the organic

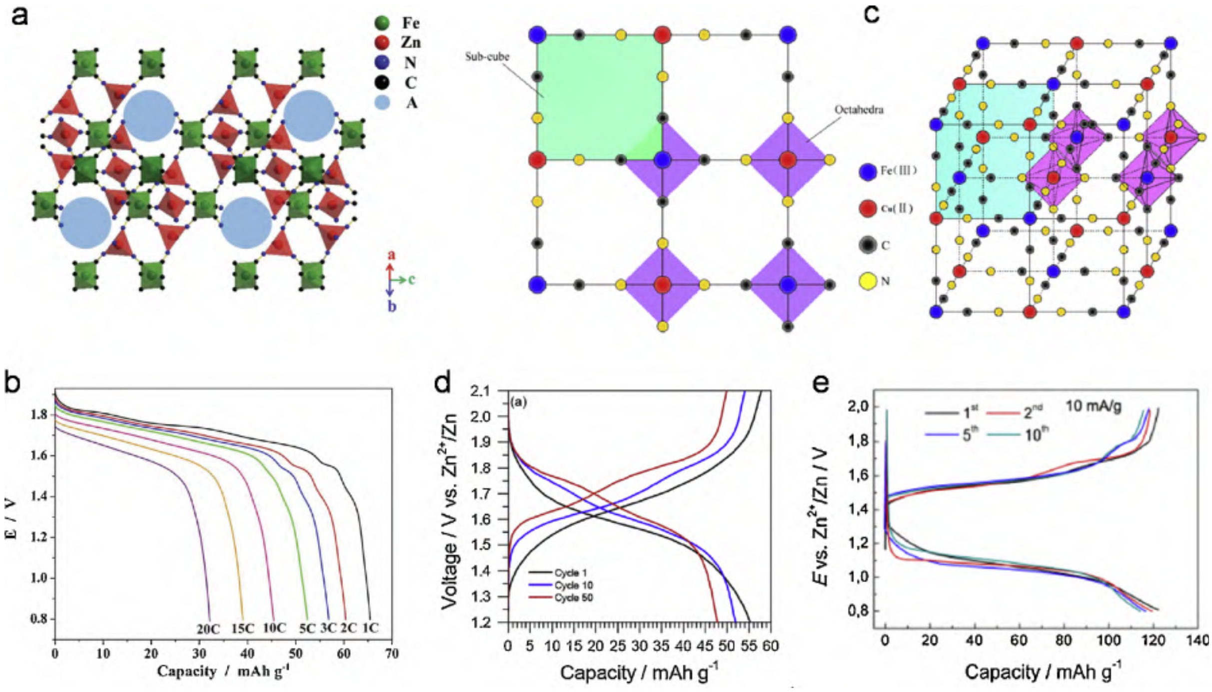

Fig. 21. Zn^{2+} (de-)intercalation behaviors within the PBA cathodes. (a) Crystal structure and (b) rate capability of rhombohedral zinc hexacyanoferrate (ZnHCF). (c) Framework and (d) galvanostatic charge-discharge profiles of copper hexacyanoferrate (CuHCF). **(e)** Galvanostatic charge-discharge profiles of ferric hexacyanoferrate (FeHCF). Reproduced with permission [89,92,94,96].

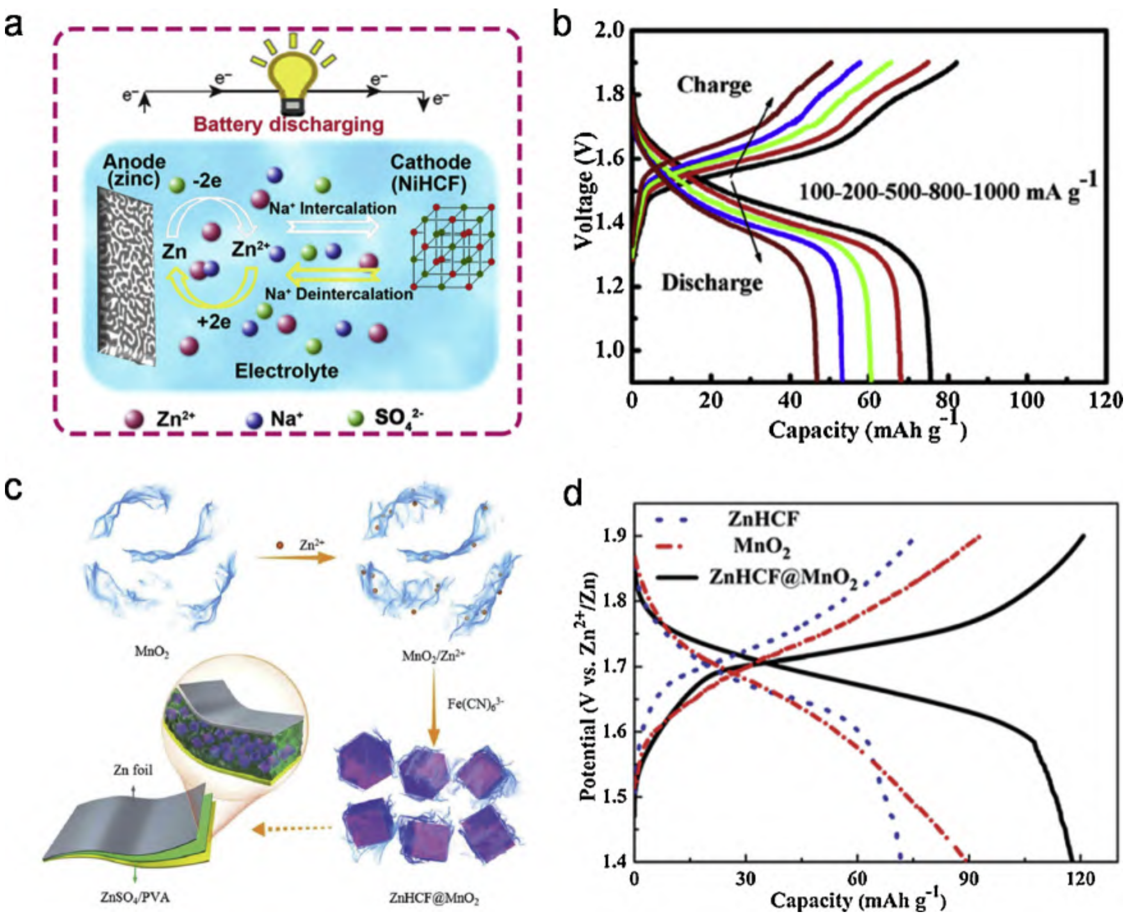

Fig. 22. Strategies to improve performance of PBA cathodes. (a) Schematic illustration of the redox process for the NiHCF//Zn battery and (b) charge and discharge curves at different current densities. (c) Schematic diagram for the fabrication procedures of the ZnHCF@MnO_2 composite and the flexible solid-state Zn-ion battery consisting of a ZnHCF@MnO_2 cathode, a $ZnSO_4$/PVA gel electrolyte, and a Zn foil anode. (d) Comparative charge-discharge curves of different materials tested under the same conditions. Reproduced with permission [99,100].

solvents acetonitrile (AN) and propylene (PC)/dimethylsulfoxide (DMSO) were used with several cathodes, including δ-MnO_2 [40], KNF-086 [97], $ZnAl_xCo_{2-x}O_4$ [101], $ZnNi_xMn_xCo_{2-2x}O_4$ [104], and $Zn_xMo_{2.5+y}VO_{9+z}$ [110].

In addition to the choice of solvent and salt, other effects are important for obtaining optimal ZIB performance: i) the salt effect, such as the difference in de-association/coordination behaviors for different salts (e.g., $ZnSO_4$ and $Zn(CF_3SO_3)_2$); ii) the concentration effect, where the electrolyte concentration can affect electrode performance; iii) the solvent effect, including the different solvation capabilities and resultant ZIB performance in aqueous and non-aqueous electrolytes; iv) the additive effect, such as $MnSO_4$ [61], $Mn(CF_3SO_3)_2$ [34], and Na_2SO_4 [116], and; v) a concentrated electrolyte, such as the "water-in-salt" concept to design electrolytes [15].

The comparative difference between $ZnSO_4$ and $Zn(CF_3SO_3)_2$ was presented in the cathode of cation-deficient spinel $ZnMn_{1.86}Y_{0.14}O_4$ [35]. Compared to the salt of $ZnSO_4$, a higher reversibility and faster kinetics of Zn deposition/dissolution were observed in the electrolyte containing $Zn(CF_3SO_3)_2$. The superior performance could be attributed to the bulky $CF_3SO_3^-$ anions (vs. SO_4^{2-} with a double charge) that decrease the number of water molecules surrounding Zn^{2+} cations and reduce the solvation effect, thereby facilitating Zn^{2+} transportation and charge transfer (Fig. 25a–c). Furthermore, the concentration of salt can significantly affect performance, and this can be optimized depending on the specific properties of the electrode (Fig. 25d) [35]. In addition to the effect of salt and concentration, different electrochemical behaviors can also be observed in aqueous and non-aqueous electrolytes. For example, the $V_3O_7{\cdot}H_2O$ cathode delivers a high capacity of 375 mA h g^{-1} at 1 C in an aqueous electrolyte containing $Zn(CF_3SO_3)_2$, while only a low capacity of 60 mA h g^{-1} and slow rate capabilities could be delivered in a non-aqueous electrolyte using AN (Fig. 14c, Fig. 25e) [77]. The reason for this difference could be the different de-solvation energy of Zn^{2+} on the electrode surface, where the type and number of molecules around Zn^{2+} are different. However, this result does not mean that the aqueous electrolyte is always better than the non-aqueous one, as we have to consider the interplay between the electrolyte and electrode.

The $ZnSO_4$ aqueous solution is the most commonly used electrolyte due to its low cost and stability, even though in some cases a better performance was obtained using a $Zn(CF_3SO_3)_2$ aqueous solution [35]. Fortunately, the addition of $MnSO_4$ can significantly improve the stability and capacity of ZIBs, particularly for the Mn-based cathode (Fig. 25f) [25]. The positive additive effect was also demonstrated in the case of β-MnO_2 using 0.1 M $Mn(CF_3SO_3)_2$ in $Zn(CF_3SO_3)_2$ (Fig. 25g) [34]. Most researchers consider that the presence of Mn^{2+} or Na^+ species in an electrolyte can alleviate the dissolution of cathode materials [116]; however, more detailed studies are required.

In addition to the study of salt, solvent, moderate concentration, and additives, a super-concentrated electrolyte (e.g., 1 M $Zn(TFSI)_2$, 20 M LiTFSI aqueous solution) was also recently developed for high reversibility of a zinc anode in stripping/plating, in which superior performances were demonstrated in a Zn/$LiMn_2O_4$ hybrid battery (Fig. 26a) [15]. This concentrated electrolyte idea originated from the recently reported "water-in-salt" concept [56], in which the V_2O_5 cathode was stabilized in hybrid ZIBs. Note that the concentrated or "water-in-salt" electrolyte concept follows similar development in LIBs

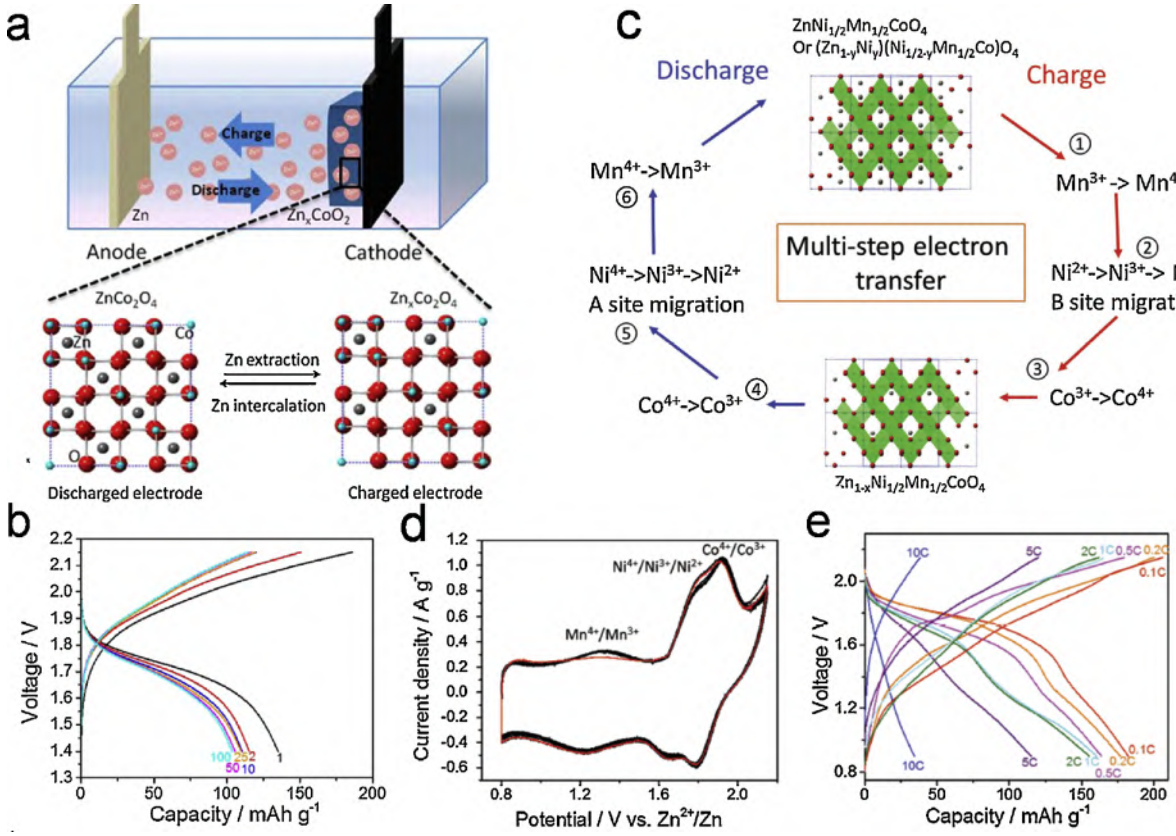

Fig. 23. Zn^{2+} (de-)intercalation behavior within new spinel oxide cathode. (a) Schematic of the Zn-ion battery using a $ZnAl_xCo_{2-x}O_4$ cathode. (b) Typical charge-discharge curves at a 0.2 C rate for $ZnAl_xCo_{2-x}O_4$ ($x = 0.67$). (c) Schematic charge and discharge processes for a $ZnNi_{1/2}Mn_{1/2}CoO_4$ electrode. Zn/Ni: silver, O: red, Mn/Ni/Co: green. (d) CV cycles for $ZnNi_{1/2}Mn_{1/2}CoO_4$, with initial cycles in red. (e) Typical charge-discharge curves at different C rates. Reproduced with permission [101,104]. (For interpretation of the references to colour in this figure legend, the reader is referred to the web version of this article).

because it can improve the electrode stability [117,118] and/or widen the electrochemical stability window of aqueous electrolytes [119].

3.2. Electrolyte characterization

The design of an appropriate electrolyte for ZIBs must take into account the cathode, the anode, and even the current collector. However, there is no “guiding principle” that can be followed in ZIBs at present, since most researchers use $ZnSO_4$ or $Zn(CF_3SO_3)_2$ electrolytes, in which the additives, salt, solvent, and concentration were optimized based on trial and error [54]. For the cathode, we can identify the electrochemical performance (vs. the zinc anode) in ZIBs to determine which electrolyte works best, whereas for the anode, the plating/stripping process and the Coulombic efficiency (CE) of zinc were studied in the electrolyte. For example, a high reversibility and stability of the Zn anode were demonstrated in a concentrated electrolyte using a Zn/Zn symmetric cell under galvanostatic conditions (Fig. 26a), where a dense, ZnO-free, and dendrite-free Zn anode was demonstrated even after 500 cycles [15]. Furthermore, the intrinsic properties of the electrolyte (e.g., Zn^{2+} solvation structures) were investigated and correlated with the electrode performance (Fig. 26b). Several characterization methods such as Fourier-transform infrared spectroscopy (FITR), the ^{18}O- NMR of water (Fig. 26c), and a Raman spectrum were used to collect the variation of binding information coordinated with cations (e.g., Zn^{2+}). Meanwhile, the solvation shell of Zn^{2+}, the coordination numbers (Fig. 26d-e), the anodic stability (Fig. 26f), the binding energy of Zn^{2+} with solvent and anions, the hydration-free energy, and the de-solvation energy of Zn^{2+} (Fig. 26g) were calculated by molecular dynamics (MD) simulations [97] and Arrhenius equations through charge transfer resistance (R_{CT}) [77]. In addition, Burrell *et al.* presented work on the stability and electrochemical window, ionic conductivity, diffusion coefficient, and Zn^{2+} transference number in different types of electrolytes, which were measured by electrochemical analysis and simulations [120].

4. Zinc anode, current collector, and separator design

For the anode in ZIBs, most researchers use zinc foil directly, while few studies have used a home-made zinc anode. In addition to the common zinc foil, other different forms were used, including the mixture of zinc powers, a conductive carbon and binder casted on a conductive support layer [20,90,95], zinc foil [27], or a freestanding thin layer [86]. In addition, zinc nanoparticles electrodeposited on a 3D, porous, nitrogen-doped carbon cloth (N − CC) substrate were used as the anode versus the cathode of MnO_2 nanorod arrays [28]. Furthermore, novel zinc anodes were also synthesized via electroplating with organic additives (e.g., cetyltrimethylammonium bromide [CTAB], sodium dodecyl sulfate [SDS], polyethylene-glycol [PEG-8000], and thiourea [TU]) in the plating solution [121]. Each additive produces a distinct crystallographic orientation and surface texture, where the electrodeposited zinc using organic additives all exhibit 6–30 times lower corrosion currents, lower float currents and higher capacity retentions than the commercial zinc foil in the hybrid Zn/$LiMn_2O_4$ aqueous battery (Fig. 27a). In particular, Zn-SDS was confirmed to be the most suitable due to its low corrosion rate, low dendrite formation, low float current, and high capacity retention after 1000 cycles. In addition to the organic additives, the effect of inorganic additives (e.g., indium sulfate, tin oxide, and boric acid) during Zn electrodeposition were studied [122], where the corrosion currents on the synthetic zinc surface decreased by 11 times, and the float charge current density

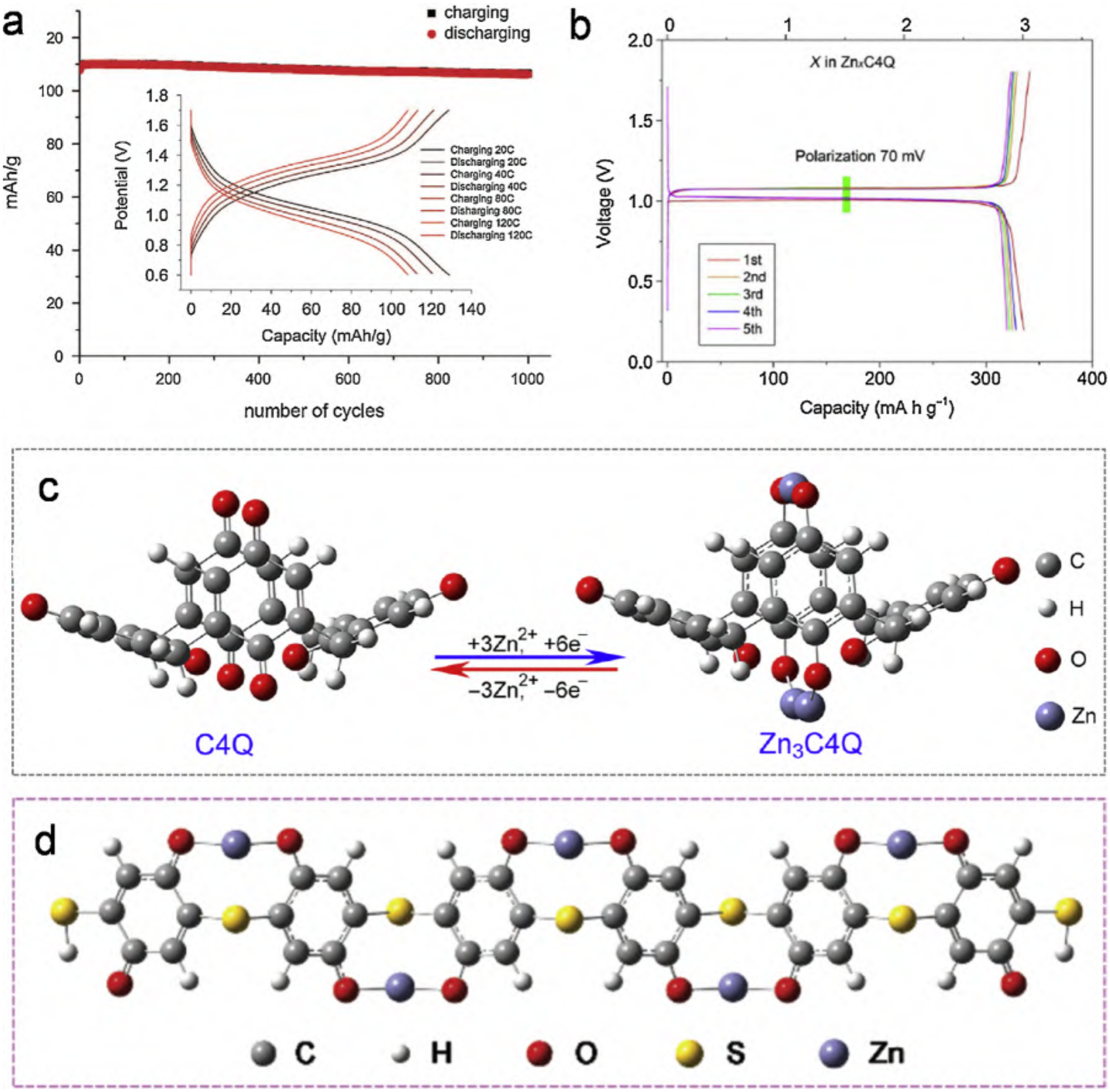

Fig. 24. Reaction of Zn^{2+} with organic cathode. (a) The capacity development during extended charge/discharge cycling of a zinc-organic hybrid battery using an exTTF cathode. (b) Galvanostatic discharge/charge curves of a Zn-C4Q battery at the current density of $20\,mA\,g^{-1}$. The upper x axis represents the uptake number of Zn ions. One Zn^{2+} with two electron transfers generates a specific capacity of $112\,mA\,h\,g^{-1}$. (c) Optimized configurations of C4Q before and after Zn-ion uptake. (d) The optimized structure of a segment on the PBQS chain after combination with Zn. Reproduced with permission [105,106,108].

decreased threefold (Fig. 27b). Meanwhile, the electrodeposited zinc anode demonstrated a higher capacity retention in the model of the Zn/$LiMn_2O_4$ aqueous battery. Besides, engineering zinc anode on nanoscale has also attract considerable interest because the designed shape, morphology, pattern and curvature can affect the final zinc anode performance, and can be utilized for various specific applications. For example, Zn array anode was fabricated onto conductive porous graphene foam via electro-deposition and applied to configure a high-rate and ultrastable flexible quasi-solid-state ZIB [83].

The selection of a current collector is critical in ZIBs for practical applications. In commercial LIBs, the cathode and anode can be cast on flexible aluminum and copper foil, respectively, for manufacturing the batteries. However, these two types of current collectors are not suitable for ZIBs because of the mild acidic environment in the electrolyte. Therefore, a steel foil or mesh [20–24,26,27,36,38,39,43,44,62,65,69,73,75,80,90,106,108], a titanium foil or mesh [34,35,56,57,64,71,86,106], a nickel grid or foam [37,85,100], carbon sheets [25,55,89,92], a carbon cloth [28,42,91,95], carbon paper [32,41,104], carbon-coated aluminum [40], carbon-coated steel [97,109], and graphite foil [94,105] have been widely used as current collectors to support the cathode, or the cathode was prepared as a freestanding film [61,76,77,79] or pellet [29,84,101] directly without the current collector (Fig. 27c). The mass loading of the cathode has mostly been kept around $5\,mg\,cm^{-2}$, and for the zinc anode, the zinc foil can fortunately be used as the anode and current collector directly in most ZIBs. However, the possible corrosion issue of zinc needs to be investigated because the amount of zinc has to be strictly controlled, considering its weight and cost in applications. On the other hand, the separator is another important component in batteries to separate electrodes and prevent shorting; more than 98% of studies on ZIBs use glass fiber or filter paper (Fig. 27d-e). Only a few studies have used a polymer-based separator such as Celgard [79,101,104] and Nafion membrane [106]. To date, there is a lack of systematic studies of separator materials in ZIBs. It is easy to understand the good compatibility of glass fiber and an aqueous electrolyte; however, the glass fiber is fragile and not as flexible as polymer-based separators. While the effect of separator

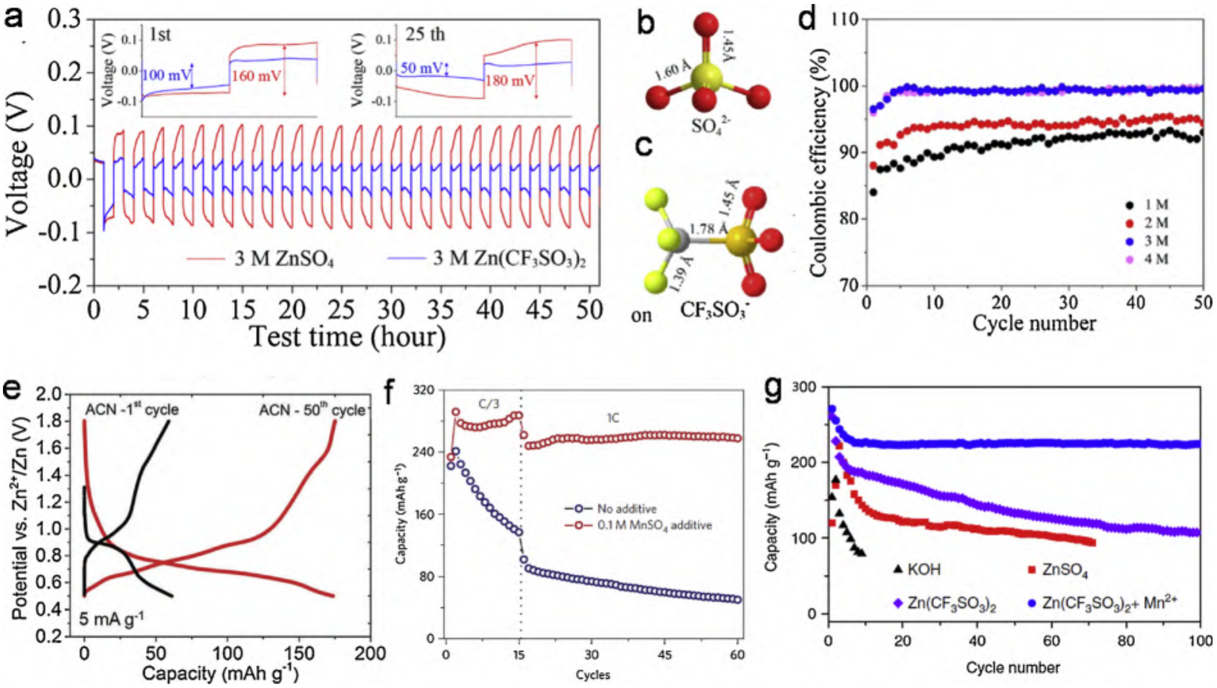

Fig. 25. Electrolyte effect on the performances of ZIBs. (a) Galvanostatic cycling of Zn/Zn symmetrical cells in 3 M $ZnSO_4$ and 3 M $Zn(CF_3SO_3)_2$ electrolytes. Insets enlarge the voltage profiles of the first and 25th cycles. Different anions of (b) SO_4^{2-} and (c) CF_3SO_3-. (d) Comparative CE of a $ZnMn_2O_4$ electrode using an electrolyte with different concentrations of $Zn(CF_3SO_3)_2$. (e) Charge/discharge polarization curves of a $V_3O_7{\cdot}H_2O$ electrode in a non-aqueous electrolyte. (f) Comparative cycling performance of α-MnO_2 electrodes with and without 0.1 M $MnSO_4$ additive in a 2 M $ZnSO_4$ aqueous electrolyte at C/3 and 1C, respectively. (g) Comparison of the cycling performance of Zn/β-MnO_2 cells with electrolytes of 45 wt.% KOH (at 0.32 C), 3 M $ZnSO_4$, 3 M $Zn(CF_3SO_3)_2$, and 3 M $Zn(CF_3SO_3)_2$ with 0.1 M $Mn(CF_3SO_3)_2$ additive at 0.65 C. Reproduced with permission [25,34,35,77].

compositions on battery performance may be not be as critical as electrolytes, researchers must address this issue for the successful commercialization of ZIBs.

5. Applications

The energy density of ZIBs, calculated assuming Mn-based and V-based cathodes, can reach as high as 85 Wh/kg and 75 Wh/kg, respectively, using assumptions similar to those used in LIBs [123]. These values are comparable to those of a Ni-H battery and are much higher than 30 Wh/kg for lead-acid batteries. Although these energy densities are smaller than the 180–230 W h/kg of LIBs, the safety, low cost, and environmental friendliness of ZIBs are sufficient incentives to adopt ZIBs in some applications. There has recently been a trend to develop flexible batteries because of the rapid growth in wearable devices, which require a reliable and safe energy storage unit. This could be an excellent opportunity for ZIBs. As illustrated in Fig. 28, the number of research papers on flexible batteries increased from 11 in 2010 to 253 in 2017, with 188 published in the last six months alone. Up to know, two types of flexible ZIBs have been reported, including standard [30,31,83,114] and hybrid ZIBs [124]. The main component to fabricate a successful, flexible ZIB is preparing a good gel polymer electrolyte (GPE). The gel electrolyte in ZIBs was actually used for the first time in 2003, where GPE films consisting of poly(vinylidenefluoride) (PVDF), propylene carbonate (PC), ethylene carbonate (EC), and zinc trifluoromethane sulfonate (ZnTFSI) were prepared and characterized using a γ-MnO_2 cathode [37]. Later, an extremely safe and wearable solid-state ZIB comprising a gelatin/polyacrylamide (PAM)-based hierarchical polymer electrolyte (HPE) and an α-MnO_2 nanorod/carbon nanotube (CNT) cathode was introduced (Fig. 29a-b) [30]. This type of electrolyte was further extended to stretchable yarn ZIBs, in which the MnO_2 cathode and zinc anode were both coated on the CNT yarn (Fig. 29c-e) [31]. Interestingly, the capacity of these two types of flexible batteries could reach 250–300 mA h g^{-1}, and their cycle life could reach more than 500 cycles with a high capacity retention. These performances are much better than those reported previously in coin cells, and the reason should be explored. More importantly, benefiting from the flexible features, these batteries could be widely applied in wearable devices, such as smart watches, fitness tracking devices, and wearable and implantable medical devices (Fig. 29f–j). Recently, a high-rate and stable quasi-solid-state zinc-ion battery with novel 2D layered zinc orthovanadate array was also reported [83]. This was the first application of V-based cathode in flexible ZIBs.

As mentioned before, the voltage window of ZIBs has much room to improve. Therefore, hybrid, flexible ZIBs, using lithium manganese oxide ($LiMn_2O_4$, LMO) and lithium iron phosphate ($LiFePO_4$, LFP) as cathodes, were reported, in which Pluronic hydrogel electrolytes (PHEs) consisting of a Pluronic polymer (F77, PEO_{53}-PPO_{34}-PEO_{53}) and an aqueous solution of mixed salts (0.25 M $ZnSO_4$ and 0.25 M Li_2SO_4) were used [124]. As a results, high voltages of 1.8 V and 1.18 V were obtained for the hybrid Zn/PHE/LMO and Zn/PHE/LFP, respectively. Using these batteries, a wearable, self-charging system, which integrated flexible ZIBs and solar cells (or other energy harvesters), was successfully demonstrated; this highlights the vast potential of ZIBs for wearable applications (Fig. 30).

6. Summary and perspective

6.1. Cathode

Significant advances have been made in the developments of cathode materials for ZIBs in the past two decades. Nonetheless, there are still many missing details that are yet to be revealed. For example, the reaction mechanism of Mn-based cathodes remains controversial, where the variation in the Mn oxidation state is still not clear (e.g., $Mn^{4+}\rightarrow Mn^{3+}$, or $Mn^{4+}\rightarrow Mn^{2+}$, or both). The realized capacity of MnO_2 cathodes, which is around 240 mA h g^{-1}, and the voltage window at ~1.3 V are attractive; however, more work is needed to

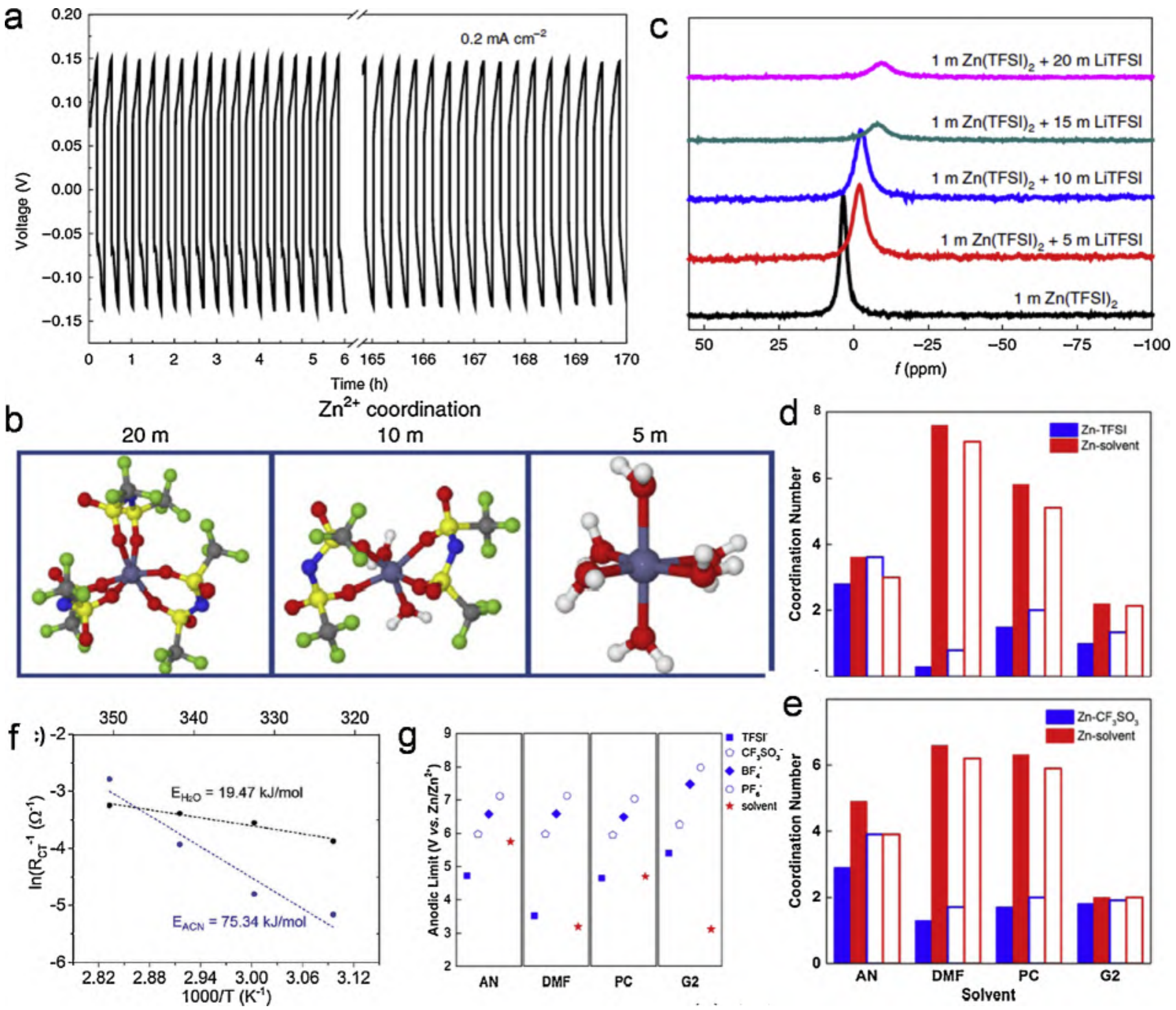

Fig. 26. Electrolyte characterizations in ZIBs. (a) Galvanostatic Zn stripping/plating in a Zn/Zn symmetrical cell. (b) Chemical shifts for ^{17}O NMR in solvent (water) as the salt concentration is varied. (c) Representative Zn^{2+}-solvation structures in electrolytes with 1 M $Zn(TFSI)_2$ and three concentrations of LiTFSI (5 M, 10 M, and 20 M). Coordination numbers of Zn anion and Zn solvent in the first solvation shell for the (d) $Zn(TFSI)_2$ and (e) $Zn(CF_3SO_3)_2$ electrolytes with four different solvents (0.1 M [filled bars] and 0.5 M [hollow bars] concentrations). (f) Arrhenius plots of inverse $R_{CT}(R_{CT}{}^{-1})$ values at different temperatures for a working electrode. (g) Calculated electrochemical windows (vs. Zn/Zn^{2+}) of different salt anions in different solvent dielectric media. Reproduced with permission [15,77,120].

reach consensus on the operating mechanism of Mn-based cathodes in ZIBs, especially the relationship between the Mn oxidation state variation and the voltage plateaus. This is critical both for understanding the electrode evolution and in order to develop strategies to improve electrode performance. In addition, the method of preparing Mn-based cathodes has to be standardized because a single phase of MnO_2 is much easier and safer for practical applications. Meanwhile, the occurrence of multi-phases in the cathode and their effect on performance has to be more fully understood. Furthermore, the temperature effect on the electrochemical performance of ZIBs must be considered more carefully, since the dissociation of H_2O ($H_2O \leftrightarrow H^+ + OH^-$) and the de-association of the Zn^{2+} solvation structure are a function of temperature. In addition, more *in-situ* characterization techniques such as *in-situ* TEM need to be utilized to reveal the reaction process in detail.

In contrast, V-based cathodes have good stability and a higher capacity, beyond the theoretical value, due to the capacitive contribution—a point that is rarely discussed in Mn-based cathodes. In addition, the moderate voltages of around 0.6-0.8 V for V-based cathodes need to be improved. Although a consensus seems to be developing about the Zn^{2+} (de-)intercalation mechanism within V-based compounds, the details of the capacitive contribution are lacking.

Furthermore, the nature of the electrode/electrolyte interphase in ZIBs needs to be studied in more detail. The relationship between the cathode structure, morphology, vacancies, and electrochemical performances must be linked together. In addition, only less than 30 chemical compounds have been introduced in ZIBs up to now (Fig. 12), while hundreds of V-based compounds with layers or tunnels remain to be explored. For the PBA cathodes, improving the cycling stability by either modifying the electrolyte or increasing the robustness of their crystalline structure remains challenging even though they exhibit an attractive voltage window of approximately 1.2–1.73 V.

The introduction of spinel oxides such as $ZnAl_xCo_{2-x}O_4$ and $ZnNi_xMn_xCo_{2-2x}O_4$ opens a new avenue to design cathodes with a high capacity and a higher voltage. However, these are some of the least studied ZIB cathodes, and more compounds should be investigated and mechanistic studies conducted. Finally, organic cathodes have attracted great attention because of their long lifespan; however, their flammability is a serious issue, and their compatibility with zinc anodes needs to be carefully considered. In fact, a stable polymer-based organic electrode has good potential for flexible battery applications because the flexible molecule has a much higher machinability in production and better compatibility in deformation conditions for wearable devices. Finally, we need to gain more insight into Zn^{2+} behavior within the cathode and at the cathode-electrolyte interface through detailed

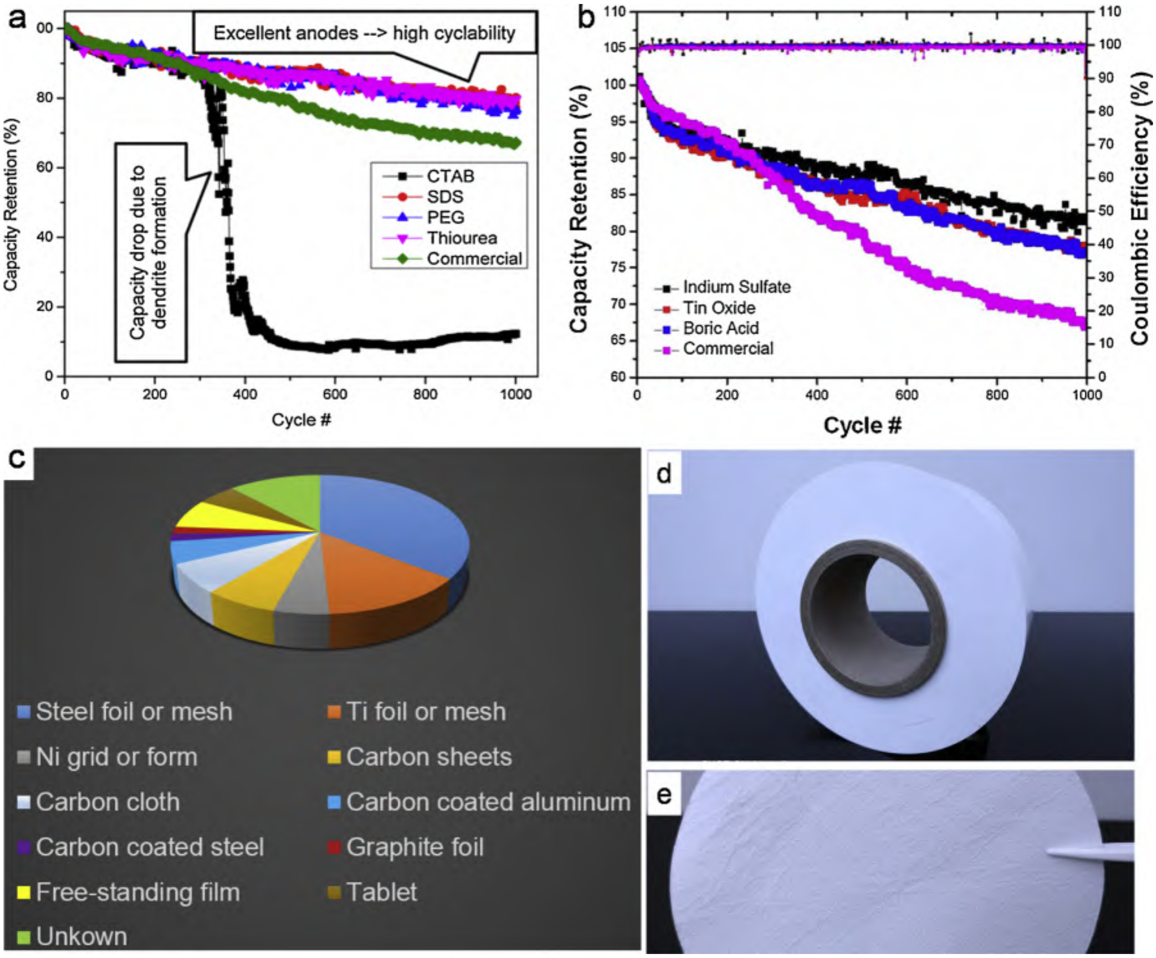

Fig. 27. Zinc anode, current collector, and separator design for ZIBs. Performances of battery using a zinc anode with (a) organic and (b) inorganic additives and commercial zinc foil. (c) Types of current collectors and the form of cathode. (d, e) Comparative Celgard microporous membrane and glass fiber. Reproduced with permission [121,122].

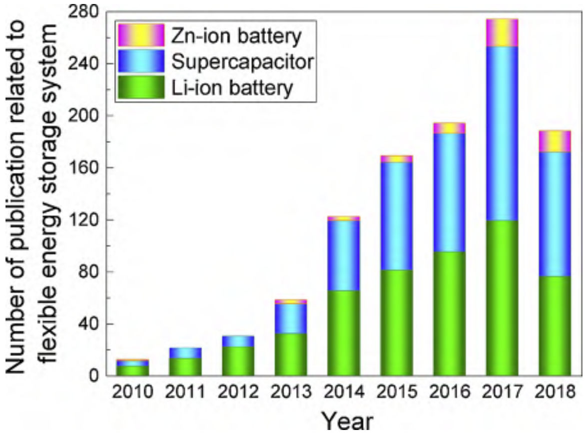

Fig. 28. Number of publications on flexible batteries and ZIBs reported in the period from 2010 to 2018.

characterization and simulations. In addition, strategies need to be developed to detect and distinguish H^+ intercalation in the Zn^{2+} (de-)intercalation process in aqueous electrolytes and Zn-intercalated compounds.

6.2. Electrolyte

For the electrolyte, the compatibility of electrolytes with zinc anodes and cathodes should be the first consideration. Then, fundamental studies are required to understand the electrolyte properties and behaviors. The cation's solvation structure, $Zn^{2+}(\text{solvent})_x(A)_y(B)_z$ (x, y, and z are coordination numbers; A represents anions from solute; and B denotes additives), provides a link between molecular-level interactions and electrolyte properties. These interactions can directly affect the zinc-ion diffusion coefficient, ionic conductivity, oxidation/reduction potential, and stripping/plating of zinc, and they should therefore be systematically characterized. The information on solvation structure could thus be collected by spectroscopy (e.g., FTIR, Raman) and simulated by MD simulation. In addition, electrolyte properties such as the stability, electrochemical window, ionic conductivity, diffusion coefficient, and Zn^{2+} transference number need to be characterized in detail. The molecular-level interactions, such as determining how the solvent, solute, and additives work in the electrolyte, must be addressed thoroughly. Considering the difference in the Zn^{2+} solvation structure in the bulk and at the cathode-electrolyte interface regions, the coordination behaviors and the de-association of Zn^{2+} (i.e., $Zn^{2+}(\text{solvent})_x(A)_y(B)_z \leftrightarrow Zn^{2+}$ + solvent + A + B) on the interphase also need to be characterized in detail. Besides, mixed and/or multi-phase aqueous/non-aqueous electrolytes can be explored as has been recently shown for the effect of water content in electrolyte on ZIB performance [125]. This is because the solvation structure and de-solvation capacity could be tuned through the type of solvent used. Furthermore, the performance of ZIBs in aqueous electrolyte at extreme temperatures should also be studied because the aqueous electrolyte can maintain a safe liquid state (vs. non-aqueous electrolyte), so the ZIBs can work in harsh conditions.

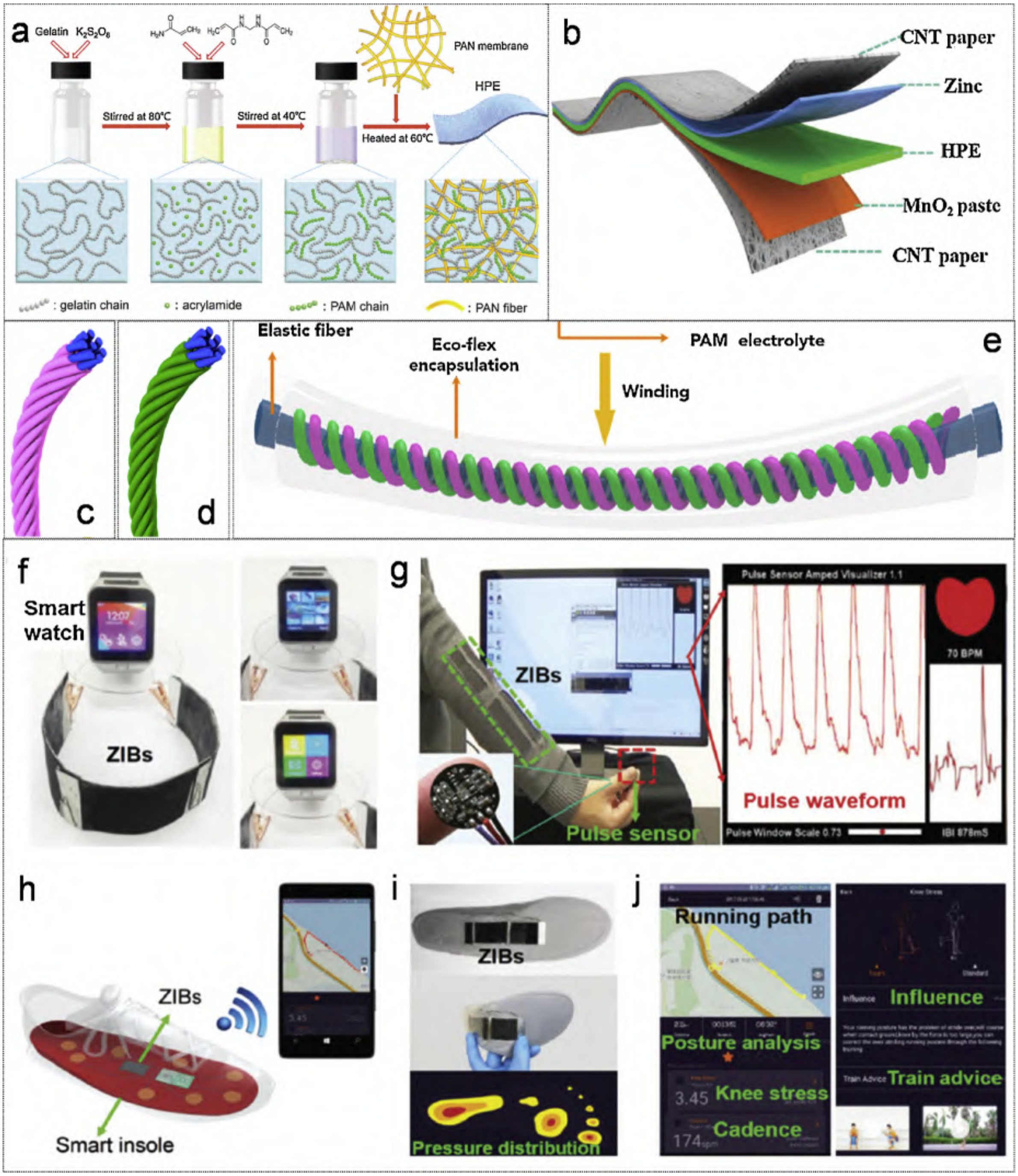

Fig. 29. A flexible and yarn-based ZIB for wearable devices. (a) Schematic depiction of the synthesis route to the HPE. (b) Schematic illustration of the structure of the solid-state flexible ZIB. (c) MnO_2-coated CNT yard. (d) Zn-coated CNT yard. (e) Schematic diagram of the fabrication and encapsulation of the yarn ZIB. (f) Three ZIBs were connected in series to power a commercial smart watch. (g) Four ZIBs were integrated in series to power a pulse sensor. (h) Schematic diagram of the ZIB-powered smart insole. (i) Optical photo of the ZIB-powered smart insole (top), the bending status of the smart insole (middle), and the pressure distribution when standing on the insole (bottom). (*j*) The running path (left) and the sport analysis results (right) obtained from the ZIB-powered smart insole. Reproduced with permission [30,31].

6.3. Anode

For the zinc anode, at least two issues should be addressed: i) the morphology and amount of zinc that should be used and ii) the corrosion rate of Zn in the electrolyte. As demonstrated in previous literature, the electrodeposited zinc exhibits better anti-corrosion and capacity retention than commercial Zn powders. However, most researchers have avoided the zinc anode problems by simply using zinc foil, which leads to both significant underutilization of the Zn anode and substantial waste. In fact, the amount of zinc anode should be controlled strictly in practical applications to maintain low-cost and high gravimetric energy density. Therefore, the corrosion rates of zinc anodes need to be studied in various electrolytes, and based on the results, the minimal required amount of zinc should be used. Furthermore, developing efficient strategies to synthesize a specialized zinc anode (e.g., electro-deposition, atomic layer deposition, thermal evaporation, etc.), to modify Zn anode surface by methods such as plasma treatment, or modify electrolytes with anti-corrosion measures

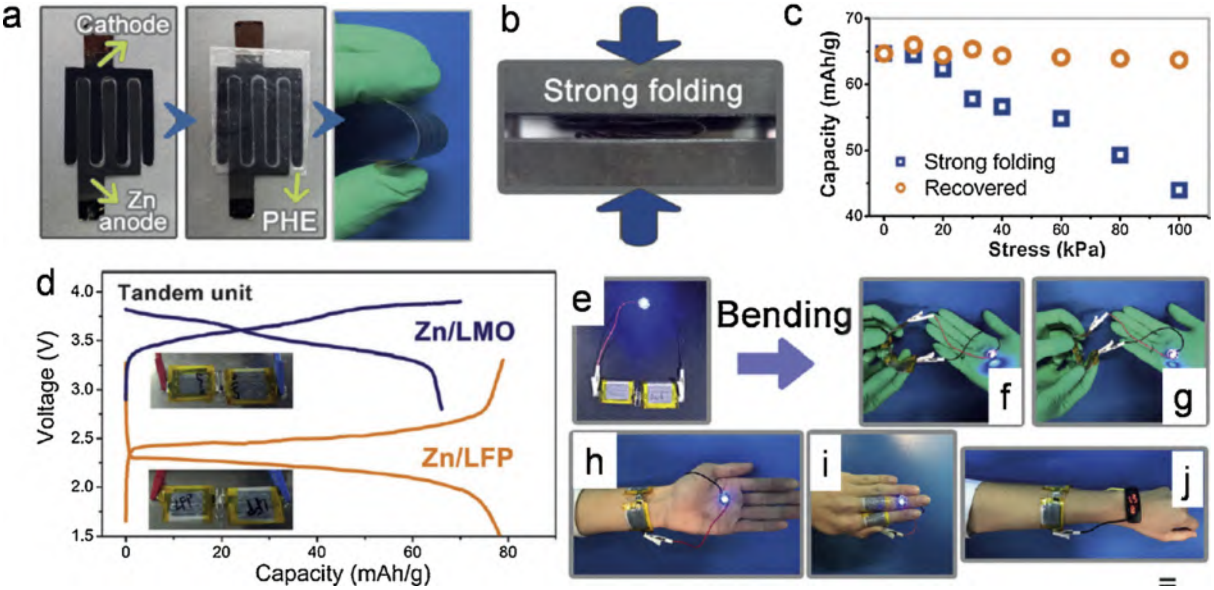

Fig. 30. A flexible hybrid ZIB. (a) Top-view and cross-sectional photographs of the flexible Zn-based battery. (b) Photographs of the flexible battery under folding. (c) Capacity change of the battery upon folding and recovering with different stresses. (d) Electrochemical performance of the tandem units with two flexible batteries in series. Photographs of the tandem unit mounted on the demonstrator's (e) wrist, (f) fingers, and (g) arm, powering (e, f) an LED and (g) a wearable watch, respectively. Reproduced with permission [124].

is necessary. The performance of zinc anodes, Zn plating/stripping behavior, Coulombic efficiency, over-potential, float charge, and current density should be characterized. Finally, we should also consider the effect of Zn anode corrosion, especially with regard to whether any H_2 is released when using a pouch cell design in particular.

6.4. Current collector

The current collector is an important component in rechargeable batteries. The current collector should be highly conductive, flexible, machinable, solderable, and relatively low-cost. However, collector engineering remains challenging even for next-generation lithium-sulfur (Li-S) and lithium-oxygen (Li-O_2) batteries due to the corrosion of the aluminum current collector in LiTFSI-based electrolytes [126] and the limited machinable or solderable properties of carbon cathodes [127] in Li-S and Li-O_2 batteries, respectively. For ZIBs, the choice of current collector may be limited; an ultrathin steel mesh or foil could be considered, while carbon cloth and carbon paper may be difficult to solder and manufacture as ultrathin film. The weight of the current collector should also be taken into account to achieve a high energy density. Furthermore, research on current collectors should also consider whether the current collector is light, low-cost, and easy to manufacture at a large scale. In addition, a direct integration of the current collector (e.g., ultrathin carbon membrane or networks with high electric conductivity) and the cathode could be an alternative strategy to solve these issues.

6.5. Separator and others

More types of separators with different compositions should be developed because of the fragility and cost of glass fiber, which has been the dominant separator used in ZIBs. A porous cellulose or hydrophilic polymer-based separator may be a choice; however, the proposed materials should be stable in mildly acidic environments and compatible with the electrode. Finally, the binder should be carefully chosen because it not only affects the utilization of active materials, but also determines how robust the electrodes will be. Therefore, more studies are required on binders for ZIBs—conductive polymers such as polyurethane, polypyrrole, polythiophene, and polystyrene can be considered.

In summary, we have reviewed the recent progress on ZIBs covering all battery components, including cathodes, electrolytes, anodes, and separators. We summarized the current performance and mechanistic understandings of ZIBs, along with their potential applications. We also identified the areas in which additional studies are required, and we presented future research directions.

Acknowledgements

Research reported in this publication was supported by King Abdullah University of Science and Technology (KAUST).

References

[1] G.Q. Li, Y. Jin, M.W. Akram, X. Chen, Renew. Sustain. Energy Rev. 79 (2017) 440–458.
[2] S. Kelly-Richards, N. Silber-Coats, A. Crootof, D. Tecklin, C. Bauer, Energy Policy 101 (2017) 251–264.
[3] G.R. Ren, J.F. Liu, J. Wan, Y.F. Guo, D.R. Yu, Appl. Energy 204 (2017) 47–65.
[4] J.M. Tarascon, M. Armand, Nature 414 (2001) 359–367.
[5] N. Nitta, F. Wu, J.T. Lee, G. Yushin, Mater. Today 18 (2015) 252–264.
[6] M.A. Hannan, M.S.H. Lipu, A. Hussain, A. Mohamed, Renew. Sustain. Energy Rev. 78 (2017) 834–854.
[7] A. Manthiram, ACS Central Sci. 3 (2017) 1063–1069.
[8] G.E. Blomgren, J. Electrochem. Soc. 164 (2017) A5019–A5025.
[9] G. Zubi, R. Dufo-López, M. Carvalho, G. Pasaoglu, Renew. Sustai. Energy Rev. 89 (2018) 292–308.
[10] M.D. Slater, D. Kim, E. Lee, C.S. Johnson, Adv. Funct. Mater. 23 (2013) 947–958.
[11] N. Yabuuchi, K. Kubota, M. Dahbi, S. Komaba, Chem. Rev. 114 (2014) 11636–11682.
[12] J.C. Pramudita, D. Sehrawat, D. Goonetilleke, N. Sharma, Adv. Energy Mater. 7 (2017) 1602911.
[13] S.B. Son, T. Gao, S.P. Harvey, K.X. Steirer, A. Stokes, A. Norman, C. Wang, A. Cresce, K. Xu, C. Ban, Nat. Chem. 10 (2018) 532–539.
[14] D. Wang, X. Gao, Y. Chen, L. Jin, C. Kuss, P.G. Bruce, Nat. Mater. 17 (2018) 16–20.
[15] F. Wang, O. Borodin, T. Gao, X. Fan, W. Sun, F. Han, A. Faraone, J.A. Dura, K. Xu, C. Wang, Nat. Mater. 17 (2018) 543–549.
[16] D.Y. Wang, C.Y. Wei, M.C. Lin, C.J. Pan, H.L. Chou, H.A. Chen, M. Gong, Y. Wu, C. Yuan, M. Angell, Y.J. Hsieh, Y.H. Chen, C.Y. Wen, C.W. Chen, B.J. Hwang, C.C. Chen, H. Dai, Nat. Commun. 8 (2017) 14283.
[17] J.A. Dean, Lange's Handbook of Chemistry (Fifteenth Edition), McGRAW-HILL, INC., New York, 1999.
[18] K. Kordesch, M. Weissenbacher, J. Power Sources 51 (1994) 61–78.
[19] C. Xu, H. Du, B. Li, F. Kang, Y. Zeng, Electrochem. Solid-state Lett. 12 (2009) A61.
[20] C. Xu, B. Li, H. Du, F. Kang, Angew Chem. Int. Ed. 51 (2012) 933–935.

[21] M.H. Alfaruqi, J. Gim, S. Kim, J. Song, J. Jo, S. Kim, V. Mathew, J. Kim, J. Power Sources 288 (2015) 320–327.

[22] B. Lee, C.S. Yoon, H.R. Lee, K.Y. Chung, B.W. Cho, S.H. Oh, Sci. Rep. 4 (2014) 6066.

[23] B. Lee, H.R. Lee, H. Kim, K.Y. Chung, B.W. Cho, S.H. Oh, Chem. Commun. 51 (2015) 9265–9268.

[24] B. Lee, H.R. Seo, H.R. Lee, C.S. Yoon, J.H. Kim, K.Y. Chung, B.W. Cho, S.H. Oh, ChemSusChem 9 (2016) 2948–2956.

[25] H. Pan, Y. Shao, P. Yan, Y. Cheng, K.S. Han, Z. Nie, C. Wang, J. Yang, X. Li, P. Bhattacharya, K.T. Mueller, J. Liu, Nat. Energy 1 (2016) 16039.

[26] M.H. Alfaruqi, S. Islam, J. Gim, J. Song, S. Kim, D.T. Pham, J. Jo, Z. Xiu, V. Mathew, J. Kim, Chem. Phys. Lett. 650 (2016) 64–68.

[27] D. Xu, B. Li, C. Wei, Y.-B. He, H. Du, X. Chu, X. Qin, Q.-H. Yang, F. Kang, Electrochim. Acta 133 (2014) 254–261.

[28] W. Qiu, Y. Li, A. You, Z. Zhang, G. Li, X. Lu, Y. Tong, J. Mater. Chem. A 5 (2017) 14838–14846.

[29] B. Wu, G. Zhang, M. Yan, T. Xiong, P. He, L. He, X. Xu, L. Mai, Small 14 (2018) e1703850.

[30] H. Li, C. Han, Y. Huang, Y. Huang, M. Zhu, Z. Pei, Q. Xue, Z. Wang, Z. Liu, Z. Tang, Y. Wang, F. Kang, B. Li, C. Zhi, Energy Environ. Sci. 11 (2018) 941–951.

[31] H. Li, Z. Liu, G. Liang, Y. Huang, Y. Huang, M. Zhu, Z. Pei, Q. Xue, Z. Tang, Y. Wang, B. Li, C. Zhi, ACS Nano 12 (2018) 3140–3148.

[32] W. Sun, F. Wang, S. Hou, C. Yang, X. Fan, Z. Ma, T. Gao, F. Han, R. Hu, M. Zhu, C. Wang, J. Am. Chem. Soc. 139 (2017) 9775–9778.

[33] S. Islam, M.H. Alfaruqi, V. Mathew, J. Song, S. Kim, S. Kim, J. Jo, J.P. Baboo, D.T. Pham, D.Y. Putro, Y.K. Sun, J. Kim, J. Mater. Chem. A 5 (2017) 23299–23309.

[34] N. Zhang, F. Cheng, J. Liu, L. Wang, X. Long, X. Liu, F. Li, J. Chen, Nat. Commun. 8 (2017) 405.

[35] N. Zhang, F. Cheng, Y. Liu, Q. Zhao, K. Lei, C. Chen, X. Liu, J. Chen, J. Am. Chem. Soc. 138 (2016) 12894–12901.

[36] J. Hao, J. Mou, J. Zhang, L. Dong, W. Liu, C. Xu, F. Kang, Electrochim. Acta 259 (2018) 170–178.

[37] G. Kumar, Solid State Ion. 160 (2003) 289–300.

[38] M.H. Alfaruqi, V. Mathew, J. Gim, S. Kim, J. Song, J.P. Baboo, S.H. Choi, J. Kim, Chem. Mater. 27 (2015) 3609–3620.

[39] M.H. Alfaruqi, J. Gim, S. Kim, J. Song, D.T. Pham, J. Jo, Z. Xiu, V. Mathew, J. Kim, Electrochem. commun. 60 (2015) 121–125.

[40] S.-D. Han, S. Kim, D. Li, V. Petkov, H.D. Yoo, P.J. Phillips, H. Wang, J.J. Kim, K.L. More, B. Key, R.F. Klie, J. Cabana, V.R. Stamenkovic, T.T. Fister, N.M. Markovic, A.K. Burrell, S. Tepavcevic, J.T. Vaughey, Chem. Mater. 29 (2017) 4874–4884.

[41] J.S. Ko, M.B. Sassin, J.F. Parker, D.R. Rolison, J.W. Long, Sustain. Energy Fuels 2 (2018) 626–636.

[42] C. Yuan, Y. Zhang, Y. Pan, X. Liu, G. Wang, D. Cao, Electrochim. Acta 116 (2014) 404–412.

[43] J. Lee, J.B. Ju, W.I. Cho, B.W. Cho, S.H. Oh, Electrochim. Acta 112 (2013) 138–143.

[44] B. Jiang, C. Xu, C. Wu, L. Dong, J. Li, F. Kang, Electrochim. Acta 229 (2017) 422–428.

[45] C. Xu, S.W. Chiang, J. Ma, F. Kang, J. Electrochem. Soc. 160 (2013) A93–A97.

[46] S. Zhao, B. Han, D. Zhang, Q. Huang, L. Xiao, L. Chen, D.G. Ivey, Y. Deng, W. Wei, J. Mater. Chem. A 6 (2018) 5733–5739.

[47] J.C. Knight, S. Therese, A. Manthiram, J. Mater. Chem. A 3 (2015) 21077–21082.

[48] N. Yabuuchi, Y. Kawamoto, R. Hara, T. Ishigaki, A. Hoshikawa, M. Yonemura, T. Kamiyama, S. Komaba, Inorg. Chem. 52 (2013) 9131–9142.

[49] P.Y. Zavalij, M.S. Whittingham, Acta Crystallographica B 55 (1999) 627–663.

[50] M. Song, H. Tan, D. Chao, H.J. Fan, Adv. Funct. Mater. (2018) 1802564.

[51] J.C. Badot, N. Baffier, J. Mater. Chem. 2 (1992) 1167–1174.

[52] D.B. Le, S. Passerini, F. Coustier, J. Guo, T. Soderstrom, B.B. Owens, W.H. Smyrl, Chem. Mater. 10 (1998) 682–684.

[53] M. Giorgetti, S. Passerini, M. Berrettoni, W.H. Smyrl, J. Synchrotron. Rad. 6 (1999) 743–745.

[54] J. Zhou, L. Shan, Z. Wu, X. Guo, G. Fang, S. Liang, Chem. Commun. 54 (2018) 4457–4460.

[55] P. Senguttuvan, S.-D. Han, S. Kim, A.L. Lipson, S. Tepavcevic, T.T. Fister, I.D. Bloom, A.K. Burrell, C.S. Johnson, Adv. Energy Mater. 6 (2016) 1600826.

[56] P. Hu, M. Yan, T. Zhu, X. Wang, X. Wei, J. Li, L. Zhou, Z. Li, L. Chen, L. Mai, ACS Appl. Mater. Interfaces 9 (2017) 42717–42722.

[57] M. Yan, P. He, Y. Chen, S. Wang, Q. Wei, K. Zhao, X. Xu, Q. An, Y. Shuang, Y. Shao, K.T. Mueller, L. Mai, J. Liu, J. Yang, Adv. Mater. 30 (2018).

[58] N. Zhang, Y. Dong, M. Jia, X. Bian, Y. Wang, M. Qiu, J. Xu, Y. Liu, L. Jiao, F. Cheng, ACS Energy Lett. 3 (2018) 1366–1372.

[59] J. Zhao, Y. Li, X. Peng, S. Dong, J. Ma, G. Cui, L. Chen, Electrochem. Commun. 69 (2016) 6–10.

[60] S. Bai, J. Song, Y. Wen, J. Cheng, G. Cao, Y. Yang, D. Li, RSC Adv. 6 (2016) 40793–40798.

[61] D. Kundu, B.D. Adams, V. Duffort, S.H. Vajargah, L.F. Nazar, Nat. Energy 1 (2016) 16119.

[62] C. Xia, J. Guo, P. Li, X. Zhang, H.N. Alshareef, Angew Chem. Int. Ed. 57 (2018) 3943–3948.

[63] Y. Oka, T. Yao, N. Yamamoto, J. Solid State Chem. 132 (1997) 323–329.

[64] P. He, G. Zhang, X. Liao, M. Yan, X. Xu, Q. An, J. Liu, L. Mai, Adv. Energy Mater. 8 (2018) 1702463.

[65] B. Tang, G. Fang, J. Zhou, L. Wang, Y. Lei, C. Wang, T. Lin, Y. Tang, S. Liang, Nano Energy 51 (2018) 579–587.

[66] L. Shan, Y. Yang, W. Zhang, H. Chen, G. Fang, J. Zhou, S. Liang, Energy Storage Mater. (2018), https://doi.org/10.1016/j.ensm.2018.08.008.

[67] O. Durupthy, N. Steunou, T. Coradin, J. Maquet, C. Bonhomme, J. Livage, J. Mater. Chem. 15 (2005) 1090–1098.

[68] Y. Mettan, R. Caputo, T. Chatterji, RSC Adv. 5 (2015) 106543–106550.

[69] M.H. Alfaruqi, V. Mathew, J. Song, S. Kim, S. Islam, D.T. Pham, J. Jo, S. Kim, J.P. Baboo, Z. Xiu, K.-S. Lee, Y.-K. Sun, J. Kim, Chem. Mater. 29 (2017) 1684–1694.

[70] P. Hu, T. Zhu, X. Wang, X. Wei, M. Yan, J. Li, W. Luo, W. Yang, W. Zhang, L. Zhou, Z. Zhou, L. Mai, Nano Lett. 18 (2018) 1758–1763.

[71] V. Soundharrajan, B. Sambandam, S. Kim, M.H. Alfaruqi, D.Y. Putro, J. Jo, S. Kim, V. Mathew, Y.K. Sun, J. Kim, Nano Lett. 18 (2018) 2402–2410.

[72] X. Guo, G. Fang, W. Zhang, J. Zhou, L. Shan, L. Wang, C. Wang, T. Lin, Y. Tang, S. Liang, Adv. Energy Mater. (2018) 1801819.

[73] Y. Cai, F. Liu, Z. Luo, G. Fang, J. Zhou, A. Pan, S. Liang, Energy Storage Mater. 13 (2018) 168–174.

[74] Z. Peng, Q. Wei, S. Tan, P. He, W. Luo, Q. An, L. Mai, Chem. Commun. 54 (2018) 4041–4044.

[75] P. He, Y. Quan, X. Xu, M. Yan, W. Yang, Q. An, L. He, L. Mai, Small 13 (2017).

[76] Q. Pang, C. Sun, Y. Yu, K. Zhao, Z. Zhang, P.M. Voyles, G. Chen, Y. Wei, X. Wang, Adv. Energy Mater. 8 (2018) 1800144.

[77] D. Kundu, S. Hosseini Vajargah, L. Wan, B. Adams, D. Prendergast, L.F. Nazar, Energy Environ. Sci. 11 (2018) 881–892.

[78] P.Y. Zavalij, F. Zhang, M.S. Whittingham, Acta Crystallographica C 53 (1997) 1738–1739.

[79] C. Xia, J. Guo, Y. Lei, H. Liang, C. Zhao, H.N. Alshareef, Adv. Mater. 30 (2018).

[80] B. Sambandam, V. Soundharrajan, S. Kim, M.H. Alfaruqi, J. Jo, S. Kim, V. Mathew, Y.-K. Sun, J. Kim, J. Mater. Chem. A 6 (2018) 3850–3856.

[81] J.H. Jo, Y.-K. Sun, S.-T. Myung, J. Mater. Chem. A 5 (2017) 8367–8375.

[82] X.Q. Wang, L.M. Liu, A.J. Jacobson, Z. Anorg. Allg. Chem. 624 (1998) 1977–1981.

[83] D. Chao, C.R. Zhu, M. Song, P. Liang, X. Zhang, N.H. Tiep, H. Zhao, J. Wang, R. Wang, H. Zhang, H.J. Fan, Adv. Mater. (2018) e1803181.

[84] P. He, M. Yan, G. Zhang, R. Sun, L. Chen, Q. An, L. Mai, Adv. Energy Mater. 7 (2017) 1601920.

[85] G. Li, Z. Yang, Y. Jiang, C. Jin, W. Huang, X. Ding, Y. Huang, Nano Energy 25 (2016) 211–217.

[86] W. Li, K. Wang, S. Cheng, K. Jiang, Energy Storage Mater. 15 (2018) 14–21.

[87] P. Barpanda, M. Ati, B.C. Melot, G. Rousse, J.N. Chotard, M.L. Doublet, M.T. Sougrati, S.A. Corr, J.C. Jumas, J.M. Tarascon, Nat. Mater. 10 (2011) 772–779.

[88] A.A. Karyakin, Electroanalysis 13 (2001) 813–819.

[89] L. Zhang, L. Chen, X. Zhou, Z. Liu, Adv. Energy Mater. 5 (2015) 1400930.

[90] L. Zhang, L. Chen, X. Zhou, Z. Liu, Sci. Rep. 5 (2015) 18263.

[91] R. Trocoli, F. La Mantia, ChemSusChem 8 (2015) 481–485.

[92] Z. Jia, B. Wang, Y. Wang, Mater. Chem. Phys. 149-150 (2015) 601–606.

[93] G. Kasiri, R. Trócoli, A. Bani Hashemi, F. La Mantia, Electrochim. Acta 222 (2016) 74–83.

[94] V. Renman, D.O. Ojwang, M. Valvo, C.P. Gómez, T. Gustafsson, G. Svensson, J. Power Sources 369 (2017) 146–153.

[95] Z. Liu, P. Bertram, F. Endres, J. Solid State Electrochem. 21 (2017) 2021–2027.

[96] Z. Liu, G. Pulletikurthi, F. Endres, ACS Appl. Mater. Interfaces 8 (2016) 12158–12164.

[97] M.S. Chae, J.W. Heo, H.H. Kwak, H. Lee, S.-T. Hong, J. Power Sources 337 (2017) 204–211.

[98] L.-P. Wang, P.-F. Wang, T.-S. Wang, Y.-X. Yin, Y.-G. Guo, C.R. Wang, J. Power Sources 355 (2017) 18–22.

[99] K. Lu, B. Song, J. Zhang, H. Ma, J. Power Sources 321 (2016) 257–263.

[100] K. Lu, B. Song, Y. Zhang, H. Ma, J. Zhang, J. Mater. Chem. A 5 (2017) 23628–23633.

[101] C. Pan, R.G. Nuzzo, A.A. Gewirth, Chem. Mater. 29 (2017) 9351–9359.

[102] S. Watanabe, M. Kinoshita, T. Hosokawa, K. Morigaki, K. Nakura, J. Power Sources 260 (2014) 50–56.

[103] K.M. Shaju, G.V.S. Rao, B.V.R. Chowdari, Electrochim. Acta 48 (2002) 145–151.

[104] C. Pan, R. Zhang, R.G. Nuzzo, A.A. Gewirth, Adv. Energy Mater. (2018) 1800589.

[105] B. Häupler, C. Rössel, A.M. Schwenke, J. Winsberg, D. Schmidt, A. Wild, U.S. Schubert, NPG Asia Mater. 8 (2016) e283.

[106] Q. Zhao, W. Huang, Z. Luo, L. Liu, Y. Lu, Y. Li, L. Li, J. Hu, H. Ma, J. Chen. Sci. Adv. 4 (2018) eaao1761.

[107] A.K. Padhi, K.S. Nanjundaswamy, J.B. Goodenough, J. Electrochem. Soc. 144 (1997) 1188–1194.

[108] G. Dawut, Y. Lu, L. Miao, J. Chen, Inorg. Chem. Front. 5 (2018) 1391–1396.

[109] M.S. Chae, J.W. Heo, S.C. Lim, S.T. Hong, Inorg. Chem. 55 (2016) 3294–3301.

[110] W. Kaveevivitchai, A. Manthiram, J. Mater. Chem. A 4 (2016) 18737–18741.

[111] G.M. Nolis, A. Adil, H.D. Yoo, L. Hu, R.D. Bayliss, S.H. Lapidus, L. Berkland, P.J. Phillips, J.W. Freeland, C. Kim, R.F. Klie, J. Cabana, J. Phys. Chem. C 122 (2018) 4182–4188.

[112] D. Kim, C. Lee, S. Jeong, IOP Confer. Ser.: Mater. Sci. Eng. 284 (2018) 012001.

[113] B. Zhang, Y. Liu, X. Wu, Y. Yang, Z. Chang, Z. Wen, Y. Wu, Chem. Commun. 50 (2014) 1209–1211.

[114] Y. Zeng, X. Zhang, Y. Meng, M. Yu, J. Yi, Y. Wu, X. Lu, Y. Tong, Adv. Mater. 29 (2017).

[115] S. Kim, J. Lee, S. Kim, S. Kim, J. Yoon, Energy Technol. 6 (2018) 340–344.

[116] F. Wan, L. Zhang, X. Dai, X. Wang, Z. Niu, J. Chen, Nat. Commun. 9 (2018) 1656.

[117] J.H. Wang, Y. Yamada, K. Sodeyama, C.H. Chiang, Y. Tateyama, A. Yamada, Nat. Commun. 7 (2016).

[118] J. Ming, Z. Cao, W. Wahyudi, M. Li, P. Kumar, Y. Wu, J.Y. Hwang, M.N. Hedhili, L. Cavallo, Y.K. Sun, L.J. Li, ACS Energy Lett. 3 (2018) 335–340.

[119] L.M. Suo, O. Borodin, T. Gao, M. Olguin, J. Ho, X.L. Fan, C. Luo, C.S. Wang, K. Xu, Science 350 (2015) 938–943.
[120] S.D. Han, N.N. Rajput, X. Qu, B. Pan, M. He, M.S. Ferrandon, C. Liao, K.A. Persson, A.K. Burrell, ACS Appl. Mater. Interfaces 8 (2016) 3021–3031.
[121] K.E. Sun, T.K. Hoang, T.N. Doan, Y. Yu, X. Zhu, Y. Tian, P. Chen, ACS Appl. Mater. Interfaces 9 (2017) 9681–9687.
[122] Kyung E.K. Sun, Tuan K.A. Hoang, The N.L. Doan, Y. Yu, P. Chen, Chem. Eur. J. 24 (2018) 1667–1673.
[123] X. Ding, X. Huang, J. Jin, H. Ming, L. Wang, J. Ming, J. Power Sources 379 (2018) 53–59.
[124] J. Zhao, K.K. Sonigara, J. Li, J. Zhang, B. Chen, J. Zhang, S.S. Soni, X. Zhou, G. Cui, L. Chen, Angew Chem. Int. Ed. 56 (2017) 7871–7875.
[125] F. Wang, W. Sun, Z. Shadike, E. Hu, X. Ji, T. Gao, X.Q. Yang, K. Xu, C. Wang, Angew Chem. Int. Ed. 57 (2018) 11978–11981.
[126] W. Wahyudi, Z. Cao, P. Kumar, M. Li, Y. Wu, M.N. Hedhili, T.D. Anthopoulos, L. Cavallo, L.J. Li, J. Ming, Adv. Funct. Mater. (2018) 1802244.
[127] H.G. Jung, J. Hassoun, J.B. Park, Y.K. Sun, B. Scrosati, Nat. Chem. 4 (2012) 579–585.